

Massive Dead Galaxies at $z \sim 2$ with *HST* Grism Spectroscopy

I. Star Formation and Metallicity Enrichment Histories

T. Morishita¹, L. E. Abramson², T. Treu³, G. B. Brammer^{1,4}, T. Jones⁵, P. Kelly⁶, M. Stiavelli¹, M. Trenti^{7,8}, B. Vulcani⁹, X. Wang³

¹Space Telescope Science Institute, 3700 San Martin Drive, Baltimore, MD 21218, USA; tmorishita@stsci.edu

²The Observatories of the Carnegie Institution for Science, 813 Santa Barbara St., Pasadena, CA 91101, USA

³Department of Physics and Astronomy, UCLA, 430 Portola Plaza, Los Angeles, CA 90095-1547, USA

⁴Cosmic Dawn Centre, University of Copenhagen, Blegdamsvej 17, 2100 Copenhagen, Denmark

⁵University of California Davis, 1 Shields Avenue, Davis, CA 95616, USA

⁶School of Physics and Astronomy, University of Minnesota, 116 Church Street SE, Minneapolis, MN 55455, USA

⁷School of Physics, Tin Alley, University of Melbourne VIC 3010, Australia

⁸ARC Centre of Excellence for All-Sky Astrophysics in 3 Dimensions, Australia and

⁹INAF – Osservatorio Astronomico di Padova, Vicolo Osservatorio 5, IT-35122, Padova, Italy

Submitted to AAS journal

Abstract

Observations have revealed $\log M_*/M_\odot \gtrsim 11$ galaxies that were already dead when the universe was only ~ 2 Gyr. Given the short time before these galaxies were quenched, their past histories and quenching mechanism(s) are of particular interests. In this paper, we study star formation and metallicity enrichment histories of 24 massive galaxies at $1.6 < z < 2.5$. A deep slitless spectroscopy + imaging data set collected from multiple *HST* surveys allows robust determination of their SEDs. Our new SED modeling provides mass accumulation/stellar metallicity enrichment histories of those galaxies over the past ~ 3 Gyr, with no functional assumptions on their star formation histories. We find that most of our massive galaxies have formed $> 50\%$ of their extant masses by ~ 1.5 Gyr before the time of observed redshifts, with a trend where more massive galaxies form earlier. Most of our galaxies already have stellar metallicities compatible with, or even higher than, those of local early-type galaxies, with a median value of $\log Z_*/Z_\odot = 0.25$ and scatter of ~ 0.15 dex. By using reconstructed star formation history, we reveal their rapid metallicity enrichment history from $z \sim 5.5$ to ~ 2.2 at a rate of ~ 0.2 dex/Gyr in $\log Z_*/Z_\odot$. The inferred metallicities are on average ~ 0.25 dex higher than observed gas-phase metallicities of star forming galaxies at the time of formation. This supports a view where quenched galaxies continue to form stars at low-level until recently, rather than abrupt termination of star formation activity.

Key words: galaxies: evolution, galaxies: formation, galaxies: star formation

1. Introduction

In the local universe, early-type galaxies dominate the massive end of the galaxy mass function, $\log M_*/M_\odot \gtrsim 11.5$ (Cole et al. 2001; Bell et al. 2003). Those galaxies consist of old and chemically enriched stellar populations, indicating most of their star formation activities ended $\gtrsim 10$ Gyr (Thomas et al. 2003; Kauffmann et al. 2003; Gallazzi et al. 2005; Treu et al. 2005a; Thomas et al. 2010). In fact, observations have revealed that some galaxies are already massive and passively evolving at $z \gtrsim 2$ (Daddi et al. 2005; van Dokkum et al. 2008; Kriek et al. 2009; Straatman et al. 2014; Belli et al. 2014; Marsan et al. 2015; Glazebrook et al. 2017). Given the short time since the Big Bang and their stellar mass, their earlier star formation must extremely be intense, followed by a rapid cessation of their star formation activity, which is often referred to as quenching.¹

However, these episodes yet remain observationally indirect — What were their star formation histories like? How and why did they stop forming stars, especially at the peak time of the cosmic star formation? Are they already enriched

in metallicity as local counterparts, or do any post-quenching processes play key roles over the following 10 Gyr? These are the central questions we aim to answer in this series of papers. In this first paper, we focus on their star formation/metallicity enrichment histories.

A number of studies have investigated star formation histories of massive galaxies in different approaches. For example, observations of high redshift galaxies provide analogy to their past properties, especially when they were actively forming stars. While sufficient valuable information can be obtained from high- z populations (e.g., star formation rate, number density, metallicity; e.g., Hamann & Ferland 1999; Tacconi et al. 2008; Toft et al. 2014), it is limited by its rather indirect aspect, where connecting different objects at different epochs may introduce systematic uncertainties (e.g., Wellons et al. 2015; Torrey et al. 2017).

Another approach is based on the archaeological information of local galaxies, or fossil record (Thomas et al. 2003; Heavens et al. 2004; Thomas et al. 2010; McDermid et al. 2015). Detailed information about their stellar population (e.g., age and chemical abundances) provides their past histories, characterizing their formation redshift to $\gtrsim 2$. This information from the local galaxies is, however, limited up to several Gyrs with current observing facilities (e.g., Worthey 1994, see also Conroy 2013), which is short for exploring star formation histories of galaxies already dead at $z \sim 2$.

¹ The term may refer to different phenomena in different contexts. For example, one may also refer to keeping star formation at very low levels after an initial decline, or the (rapid) decline of SF itself (see Man & Belli 2018, for a recent review). We use the term to describe any decline of galaxy star formation activity regardless of speed.

To explore evolution histories in the earlier epoch, we need a method that combines some of the virtues of both approaches, that is, the archaeological study of high- z galaxies. For example, Kelson et al. (2014) perform SED modeling of galaxies at $z \sim 1$ by using low-resolution spectra and broadband photometry, and reconstructed their star formation histories back to $z \sim 1.5$ (also Dressler et al. 2016, 2018). Chauke et al. (2018) recently attempted the similar approach to galaxies at $z \lesssim 1$ but with higher resolution spectra taken with a ground-based spectrograph, and successfully revealed their formation histories back to $z \sim 2.5$. In the current study, we target galaxies at higher redshift, aiming at earlier evolution histories up to their formation redshift from fossil record obtained with low-spectral resolution yet high sensitivity *HST* spectrophotometric data set.²

Stellar metallicity is another key parameter that provides further details of their evolution processes. In particular, since both the cosmic metallicity and individual gas phase metallicity are still pristine at these redshifts (e.g., Erb et al. 2006; Maiolino et al. 2008; Lehner et al. 2016), the enrichment process within such massive systems *has to be* substantial to explain the observed solar/super-solar metallicity of lower redshift galaxies (Onodera et al. 2012; Gallazzi et al. 2014; Choi et al. 2014; Lonoce et al. 2015), whereas the process is highly dependent on star formation histories (e.g., Peng et al. 2015).

With such demands, we here improve our previous methodology of SED modeling, which is free from functional forms of star formation histories, by increasing flexibility in metallicity. We collect 24 massive quenched galaxies at $z \sim 2$ that have deep WFC3/G102 and G141 grism spectra coverage in their rest-frame 4000 Å. The combination of grism spectra and wide broadband photometry (0.2 μm to 8.0 μm by *HST* and *Spitzer*) provides a unique opportunity to constrain not only age but also metallicity from the entire SED shape.

We proceed as follows. In Section 2, we describe the data used in this study and their reduction process. In Section 3, we introduce our method for the SED modeling. In Section 4, we show the results. We discuss our results and interpretation in Section 5 and close in Section 6. Further details, including a simulation test of SED modeling and comparison with functional star formation histories, are also presented in Appendices. Throughout the text, magnitudes are quoted in the AB system (Oke & Gunn 1983; Fukugita et al. 1996), and $\Omega_m = 0.27$, $\Omega_\Lambda = 0.73$, $H_0 = 72 \text{ km s}^{-1} \text{ Mpc}^{-1}$ for the cosmological parameters, and $Z_\odot = 0.0142$ (Asplund et al. 2009) for the solar metallicity.

2. Data

To achieve our goal of constraining galaxy star formation histories, it is essential to cover the wavelength range surrounding 4000 Å, where the spectral features are most age-sensitive, with sufficiently deep spectra and rest-frame NUV-optical-NIR wavelength with broad band photometry. Therefore, we limit ourselves to only fields where deep *HST* grism data are available, which are MACS1149.6+2223 (hereafter M1149) and the GOODS-North/South (GDN/GDS). To collect the initial photometric sample galaxies, we use publicly available photometric catalogs. We use *HST*/WFC3 G102 and G141 grism data (that covers $\lambda_{\text{obs}} \sim 8000 \text{ Å}$ to 17000 Å) taken in various surveys in these fields.

² Belli et al. (2018) recently presented star formation histories of $1.5 < z < 2.5$ galaxies reconstructed with ground-based spectroscopic data. None of their sample galaxies overlaps with ours in this study.

2.1. Initial Photometric Sample

M1149 is a sightline of a massive cluster of galaxies at $z = 0.544$. The data were taken in CLASH (Postman et al. 2012), Hubble Frontier Fields (HFF; Lotz et al. 2017), GLASS (Schmidt et al. 2014; Treu et al. 2015), and the SN Refsdal followup campaigns (Kelly et al. 2015, 2016). The combination of its gravitational magnification power and those very deep observations provides a unique opportunity among other clusters of GLASS. We use the photometric catalog used in Morishita et al. (2017, 2018), which consists of *HST* photometry taken in all *HST* surveys above, as well as *Spitzer* IRAC (3.6 + 4.5 μm ; Pls T. Soifer and P. Capak) and ground-based K_S -band imaging (Brammer et al. 2016) and publicly available spectroscopic redshifts by GLASS (Schmidt et al. 2014).

For GDN and GDS, we use the publicly available catalog by 3DHST (Skelton et al. 2014). The photometric catalog consists of fluxes, spectroscopic/photometric redshifts, rest-frame colors, and stellar mass, based on data taken in CANDELS and 3DHST (Grogin et al. 2011; Koekemoer et al. 2011; van Dokkum et al. 2013a; Skelton et al. 2014; Momcheva et al. 2016), as well as photometric fluxes obtained in ground-based surveys. We use *HST* photometry for optical/near-IR range, ground-based K_S -band photometry, and *Spitzer* IRAC photometry in this study. Other ground-based fluxes listed in the 3DHST catalog, most of which are in the optical range, are not used, as the deep *HST* photometry is sufficient to constrain optical SEDs.

Broadband fluxes of *HST* are measured in a fixed aperture ($r = 0.7''$) and then scaled to the total flux by multiplying $C = f_{\text{AUTO}}/f_{\text{aper}}$, where f_{AUTO} is AUTO flux of SExtractor (Bertin & Arnouts 1996), as in Skelton et al. (2014) and Morishita et al. (2017).

From these photometric catalogs, we choose those satisfy $m_{140} < 24$, $1.6 < z < 3.3$, $\log M_*/M_\odot > 10.8$. We also apply $(U - V)_{\text{rest}} > 1 \text{ mag}$ to select quiescent galaxies. By setting slightly bluer color for $U - V$ than literature ($\sim 1.4 \text{ mag}$), our sample also contains quenching galaxies too. With the criteria, we found 17, 51, and 73 galaxies in M1149, GDN, and GDS, respectively, as an initial photometric sample (Figure 1).

2.2. HST Grism Spectrum

In M1149, the grism data were taken through GLASS (Schmidt et al. 2014; Treu et al. 2015). GLASS is a spectroscopic survey with *HST*/WFC3 G102 and G141 grisms (10 and 4 orbits, respectively). In addition, we supplement with the follow-up HSTGO/DDT campaign (Proposal ID 14041, P.I. P. Kelly) of the multiply imaged supernova, SN Refsdal (Kelly et al. 2015, 2016), which add another 30 orbits of G141 data to the original GLASS observation.

In GDN/GDS, we retrieve the public data through MAST. In addition to the 3DHST data (van Dokkum et al. 2013b; Momcheva et al. 2016) that covers entire CANDELS' GDN/S fields, we add those taken in FIGS (13779; P.I. S. Malhotra Pirzkal et al. 2017), CLEAR (14227; P.I. C. Papovich, also Estrada-Carpenter et al. 2018), and other followups (12099&12461; P.I. A. Riess, 12190; A. Koekemoer, 13420; P.I. G. Barro, 13871; P.I. P. Oesch).

We extract 1D spectra from all fields in a consistent way, by using the latest version of Grizli (Brammer 2018). During the extraction, the code automatically models neighboring objects, which are flagged in pre-provided SExtractor segmentation maps, and produces clean spectra for a target galaxy. The

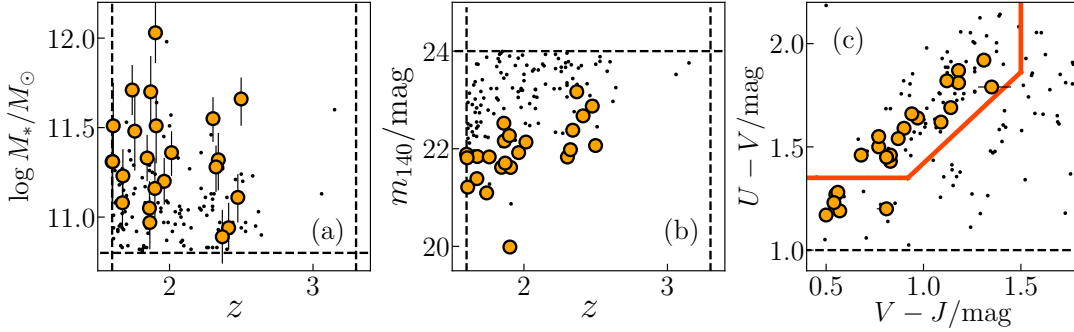


Figure 1. Physical properties of initial photometric sample galaxies (dots) and final 24 galaxies (orange circles). The criteria used for the initial photometric selection are shown with dashed lines. (a) Stellar mass distribution as a function of redshift. (b) F140W magnitude distribution as a function of redshift. (c) UVJ-color diagram. Our sample consists of both quenched (left-top region bounded by a solid line) and quenching (those $U - V > 1$ but outside the boundary) galaxies.

clean, optimal extracted spectra from each position angle (PA) is then stacked in a refined wavelength grid of $45 \text{ \AA}/\text{pixel}$. The pixel scale is slightly finer than the Nyquist sampling of G141 grism, since we have many sampling over different orbits, each of which slightly shifts in the dispersion direction. Each spectrum is convolved with the image of the source to match the morphological difference in different PAs.

For the aperture correction of broadband photometry and the grism flux, we match the pseudo broadband flux extracted from the spectra by convolving with the corresponding filters (F140W/F105W) to the observed broadband flux (Section 3.2).

In addition to the random uncertainty, we also estimate the uncertainty associated with stacking of different PAs by following Onodera et al. (2015), and integrate this to the random noise in quadrature for conservative estimates. The uncertainty accounts of $\sim 20\%$ of the random uncertainty. S/Ns of the final 1D spectrum range up to ~ 50 . Median values of each spectral element are $S/N \sim 18$ at $4200\text{--}5000 \text{ \AA}$ and ~ 4 at $3400\text{--}3800 \text{ \AA}$ (Table 1).

2.3. Additional Photometric Data

In addition to photometric fluxes collected in 3DHST, we add WFC3/UVIS photometry. The rest frame UV coverage is important to constrain SEDs with/without the UV upturn, which depends on metallicity (e.g., Yi et al. 1997; Treu et al. 2005b). We use WFC3/UVIS images from HDUV legacy survey (Oesch et al. 2018), that cover parts of GDN/GDS fields with F275W and F336W filters. The UVIS images in GDS consist of the previous data taken in the UDF by the UVUDF team (Teplitz et al. 2013). We run SExtractor on the public imaging data to conduct photometry, and use flux measured in a fixed aperture of $0''.72$ diameter.

3. Spectro-photometric SED fitting

3.1. Basic Templates

Our SED fitting method (Grism SED Fitter, or `gsf`; Morishita, in prep.) is based on the canonical template fitting, where the best fit parameters are determined by minimizing the residuals of observed and model SEDs. One major difference from most of other works is the way we construct the model templates. SED templates are often constructed with a functional form for star formation histories (SFHs), such as the exponential declining model, $\psi \propto A \exp[-(t - T_0)/\tau]$, where A , T_0 , and τ are free parameters. However, it is known that such a simplification may not represent real galaxy SFHs

by observations (e.g., Pacifici et al. 2016; Iyer & Gawiser 2017) and simulations (e.g., Diemer et al. 2017). As such, we here avoid any functional forms and adopt an alternative method to generate model templates. The core of the method is to find the best combination of amplitudes, $\{a_i\}$, for a set of composite stellar population (CSP) templates of different ages, $\{t_i\}$, that matches the data, as previously performed by Morishita et al. (2018). This type of SED modeling has been used in previous studies (Heavens et al. 2004; Cid Fernandes et al. 2005; Panter et al. 2007; Tojeiro et al. 2007; Kelson et al. 2014; Dressler et al. 2018), some of which demonstrated its strength and validity with intensive simulation tests.

To generate the template with different parameters, we use the Flexible Stellar Population Synthesis code (FSPS; Conroy et al. 2009; Conroy & Gunn 2010; Foreman-Mackey et al. 2014) to generate i th templates with ages of t_i , based on MIST isochrones (Choi et al. 2016) and the MILES stellar library. As found by Morishita et al. (2018), different isochrones may return different results, in addition to a systematic difference in assumed metallicities.

We set the number of age “pixels” to 10, with $[0.01, 0.03, 0.1, 0.3, 0.5, 0.7, 1.0, 1.5, 2.0, 3.0]$ Gyr (Figure 2), doubling the number from those adopted in Morishita et al. (2018). While we set the equal width of template in log normal space (~ 0.5) following previous studies (e.g., Cid Fernandes et al. 2005), we added extra bins at intermediate age, where most of our galaxies locate, to increase the flexibility of SFHs.

The template is generated by assuming a short constant star formation rate within each bin width ($\sim 30 \text{ Myr}$), rather than simple stellar population (SSP). The reason we do not adopt the SSP model is that, while it is simple, it is unrealistic for real galaxies. Changing the width of constant star formation in each bin would result in a minor but systematic shift in reconstructed SFHs. The uncertainty in bin width is considered in calculation of parameters (e.g., age), by randomly fluctuating values within the width.

We also set metallicity of each age pixel as a free parameter in a range of $\log Z_*/Z_\odot \in [-0.8 : 0.6]$, as opposed to one global value in Morishita et al. (2018). While determination of metallicity at each age pixel (i.e. metallicity histories of individual galaxies) is more challenging (see Appendix A), this gives extra flexibility in fitting templates, and allows reasonable estimate of uncertainty in star formation histories (Section 5.4).

It is noted that metallicity sensitive lines (such as Fe and Mg) are not measured at our spectral resolution. Our method rather relies on the entire spectral shape with grism spectra

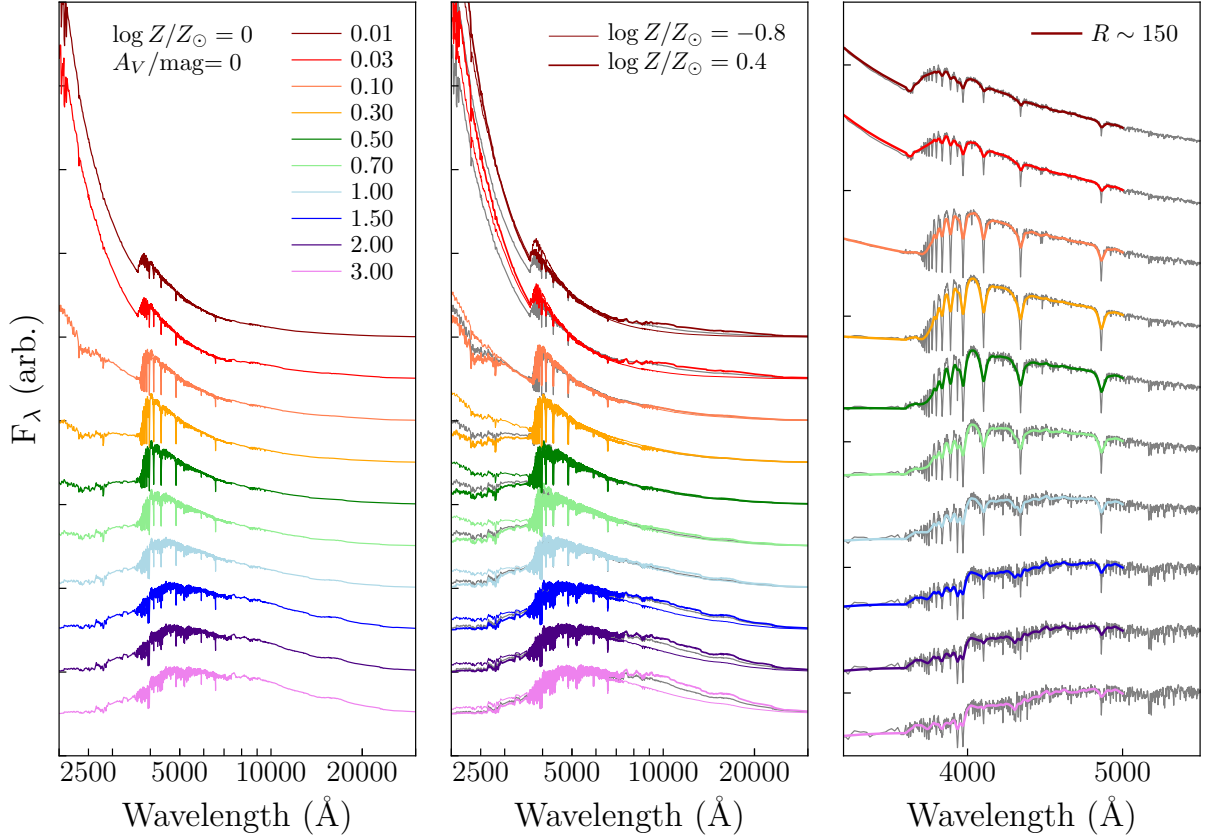


Figure 2. **Left:** Original spectral templates used in fitting. Only those with $\log Z_*/Z_\odot = 0$ without dust attenuation ($A_V = 0$) are shown here, with arbitrary shifts in flux. **Left:** Same as left panel (gray solid lines) but also showing templates with different metallicities for comparison (thin lines for $\log Z_*/Z_\odot = -0.8$; thick lines for $\log Z_*/Z_\odot = 0.4$). Templates are normalized at 5000 \AA . **Right:** Same as left panel (gray solid lines) but also showing spectra that are degraded to match the observation, that accounts for the G102/G141 resolutions and source morphology ($R \sim 150$; colored lines).

and wide broadband photometry, that spans from NUV, optical (that are sensitive to age), to NIR (to metallicity) wavelength range (see Figure 2).

Templates generated with MIST are uniformly set to the solar-scaled abundance (Asplund et al. 2009; i.e. $[\alpha/\text{Fe}] = 0$). It is noted that galaxies at high- z may have a α -enhanced chemical composition (e.g., Onodera et al. 2015; Kriek et al. 2016), as found in local early-type galaxies (e.g., Thomas et al. 2005; Walcher et al. 2015). In fact, enhancement of α -element has a similar effect as one of iron in UV and NIR continuum slopes (e.g., Vazdekis et al. 2015), while our low resolution spectra cannot capture detailed difference in each absorption line (i.e. Lick indices), and both abundances are degenerated in our total metallicity measurement, $\log Z_*/Z_\odot$.³ As such, our total metallicity should remain similar to those with e.g., α -enhanced templates (see also Walcher et al. 2009).

We assume a Salpeter (1955) IMF and Calzetti et al. (2000) dust law, where the dust attenuation, A_V , is a global parameter that is applied to all age templates equally. Redshift is set as a free parameter at this step, but within the 3σ range estimated in the previous step. In sum, the fits have $10 \times 2 + 1 + 1 = 22$ free parameters.

The degree of freedom of our fitting is worth noting. The

number of spectral data point for each of our galaxies is > 200 (with ~ 16 for broadband photometric data points), where the spectral element is set to 45 \AA in this study. Considering the correlation due to morphology (which is $\sim 104 \text{\AA}$ for the mean size of our galaxies, $r \sim 0.3''$), and the large number of parameter, our spectra still have ~ 100 independent data points.

Our updated method here has a few advantages from Morishita et al. (2018). First, it is more flexible than a-priori assumption of the star formation history, and robust to systematic bias in derived parameters (e.g., Wuyts et al. 2012). Second, it is flexible to a complex shape of SFHs, such as those with multiple bursts and sudden declines (e.g., Boquien et al. 2014). A star formation history with multiple peaks cannot be reproduced by the exponential declining model (see Section 4). Third, it is flexible to the metallicity evolution. Methods with functional forms often have a fixed metallicity over the entire history. In our method, each template at different age have a flexibility in metallicity as a free parameter, that provides metallicity enrichment histories.

3.2. SED parameter exploration

The combination of templates is controlled by changing each amplitude, a_i , as free parameters during the fit. A challenging part is the large number of parameters (over a dozen compared to $\lesssim 5$ parameters with functional SFHs), which could be trapped in local minima. To sufficiently, yet effi-

³ Total metallicity is often inferred with $[Z/H] = [\text{Fe}/H] + A[\alpha/\text{Fe}]$, where $A \sim 0.9$ depending on abundance ratios (e.g., Trager et al. 2000; Jimenez et al. 2007).

ciently, explore the parameter space, we adopt the Markov Chain Monte Carlo (MCMC) method.

The fitting process of *gsf* is two-folded — 1. initial redshift determination based on visual inspection of absorption lines, and 2. MCMC realization to estimate probability distribution for all parameters.

gsf first determine the redshift by fitting the model templates to the observed grism spectrum. At this point, it only generates model templates in the wavelength range of grism spectra, to minimize the computational cost. The templates are convolved to the resolution of the spectra with a Moffat function derived from the observed source morphology for spectra. It searches the best fit redshift by minimizing χ^2 , as well as visual inspection to avoid catastrophic errors. During the visual inspection, we rely on the major absorption lines in the observed range (i.e. $H\delta$, $H\gamma$, $H\beta$), and thus those without clear absorption features (i.e. low-S/N) are discarded here. At this step, *gsf* also determines the scale of G102/G141 spectra so that each matches to the broadband photometry in F105W and F140W at a given template. The added scale for our sample is small ($\lesssim 10\%$) thanks to the accurate sky-background estimation in Grizli.

gsf then generates a template library at the redshift determined in the previous step and fits SEDs at the entire wavelength range. *gsf* fits the observed spectra and broadband photometry simultaneously by using *emcee* (Foreman-Mackey et al. 2013) as in Morishita et al. (2018). Redshift is also explored at this step by shifting and refining the template wavelength grid at a proposed redshift of each MCMC step. Emission lines, if detected, are masked during the fit. Those lines are modeled with a gaussian function after subtracting the best fit SED template to estimate the line flux and equivalent width (Section 4.2).

We set the number of walkers to 100 and the number of realization, N_{mc} , to 10^5 . We adopt an uniform prior for each parameter over the parameter ranges, $a_i \in [0 : 1000]$, $\log Z_*/Z_\odot \in [-0.8 : 0.6]$, and $A_V/\text{mag} \in [0 : 4]$. While some of previous studies set a prior in metallicity histories from the local mass metallicity relation (e.g., Pacifici et al. 2016; Leja et al. 2018) (i.e. increasing metallicity as a function of time), we find that our result reproduce this behavior without such priors. However, the age-metallicity degeneracy could also mimic this trend. Our test with a mock data set (Appendix A) revealed, while the trend is fairly reproduced, non-negligible scatters in derived metallicity at each age pixel, and that metallicity histories of *individual* galaxies remain less promising (see also below).

During the fit, we let *emcee* run with the parallel tempering sampling, with $n_{\text{temp}} = 5$. With this, *emcee* samples the parameter spaces but with n_{temp} samplers in parallel. Each sampler has a different value for the temperature parameter in a Metropolis-Hastings step, i.e. a higher temperature makes a larger step in a parameter space. With this, the sampler suffers less from the local minima. We note however that a sufficient number of MCMC realization (which is inferred from a simulation test for our case) is necessary to estimate reliable uncertainties. Otherwise, derived uncertainties would become inappropriately small, with possible biases in the best fit values (see Cid Fernandes 2018).

The first half realization of the sampled chain is discarded to avoid biased results from initial input values. We take the 50th and 16/84th percentiles of marginalized distributions as the best fit and uncertainty range.

To check the reliability of SED parameters and reconstructed histories, we conducted a simulation test with mock data set (Appendix A). From the test, we found that the scatter in the reproduced amplitude and metallicity at each age bin are ~ 0.5 dex and ~ 0.25 dex, respectively. To account for this, we add the estimated scatter to the reconstructed star formation and metallicity histories, which are also propagated to other SED parameters (Section 4.3).

4. Results

4.1. Twenty-Four Galaxies as the Final Sample

In Figure 1, we summarize basic parameters of final sample galaxies. The final sample consists of 2, 12, and 10 galaxies from M1149, GDN, and GDS, after the rest of initial samples are visually discarded because of poor redshift fitting quality (Section 3.2). Due to the partial coverage of the grism observations, and also random contamination from neighboring galaxies, our samples have non-uniform exposure time in the grism observation and signal to noise ratio (Table 1). The two galaxies in M1149 are those previously reported by Morishita et al. (2018).

In (a) and (b), we plot the distribution of our sample galaxies in redshift-stellar mass/F140W-magnitude spaces, respectively. Due to the increasing sensitivity of G141 grism with wavelength, galaxies at higher redshift are fainter in F140W than those at lower redshift. In (c), we show the UVJ color-color diagram for diagnosing galaxy quiescence (e.g., Williams et al. 2009). While most of the sample locate within the passive category, there are 6 galaxies that fall below the passive/star forming boundary in $U - V$. These galaxies are in transition between star forming ($U - V \lesssim 1$) and passive ($\gtrsim 1.4$), akin to the green valley galaxies in the local universe (Kauffmann et al. 2003; Schawinski et al. 2014). Those transitioning galaxies are interesting target to investigate quenching mechanisms at this redshift (Barro et al. 2013, 2014; Toft et al. 2014, also Morishita in prep.).

The derived parameters are summarized in Table 1. It is noted that estimated errors in stellar mass are larger (~ 0.2 dex) than those listed in original catalogs ($\lesssim 0.1$ dex). This is due to the fact that our fitting also takes account of the uncertainty in SFHs (see also Wuyts et al. 2012; Morishita et al. 2015), while previous studies often assume a functional form for SFHs and then quote random photometric error (plus photometric redshift error) as the uncertainty of SED parameters (also Appendix B).

4.2. Diagnostics from the SED shape

In the left panel of Figure 3, we show SEDs of the sample galaxies with the best-fit templates. Our galaxies are well characterized with $k + a$ (Dressler & Gunn 1983) and quiescent spectra, as is expected from the sample selection and redshift range. Deep spectra successfully capture spectral features of these types of galaxies, such as absorption lines and 4000 Å/Balmer break. The wide broadband coverage well captures spectral features, such as a blue UV slope from a young population (~ 1 Gyr) and near-IR excess from a old population ($\gtrsim 2$ Gyr), that is consistent with the derived mass-weighted age (T_* ; see Table 1).

6 galaxies have weak emission lines detected ($\sim 1.5\sigma$), such as $[O II]$, $H\delta$, $H\gamma$, and $H\beta$, that is a signature of ongoing star formation. We first fit the emission line with a Gaussian after subtracting the best fit spectrum. The equivalent width (EW) is then measured with the total flux from

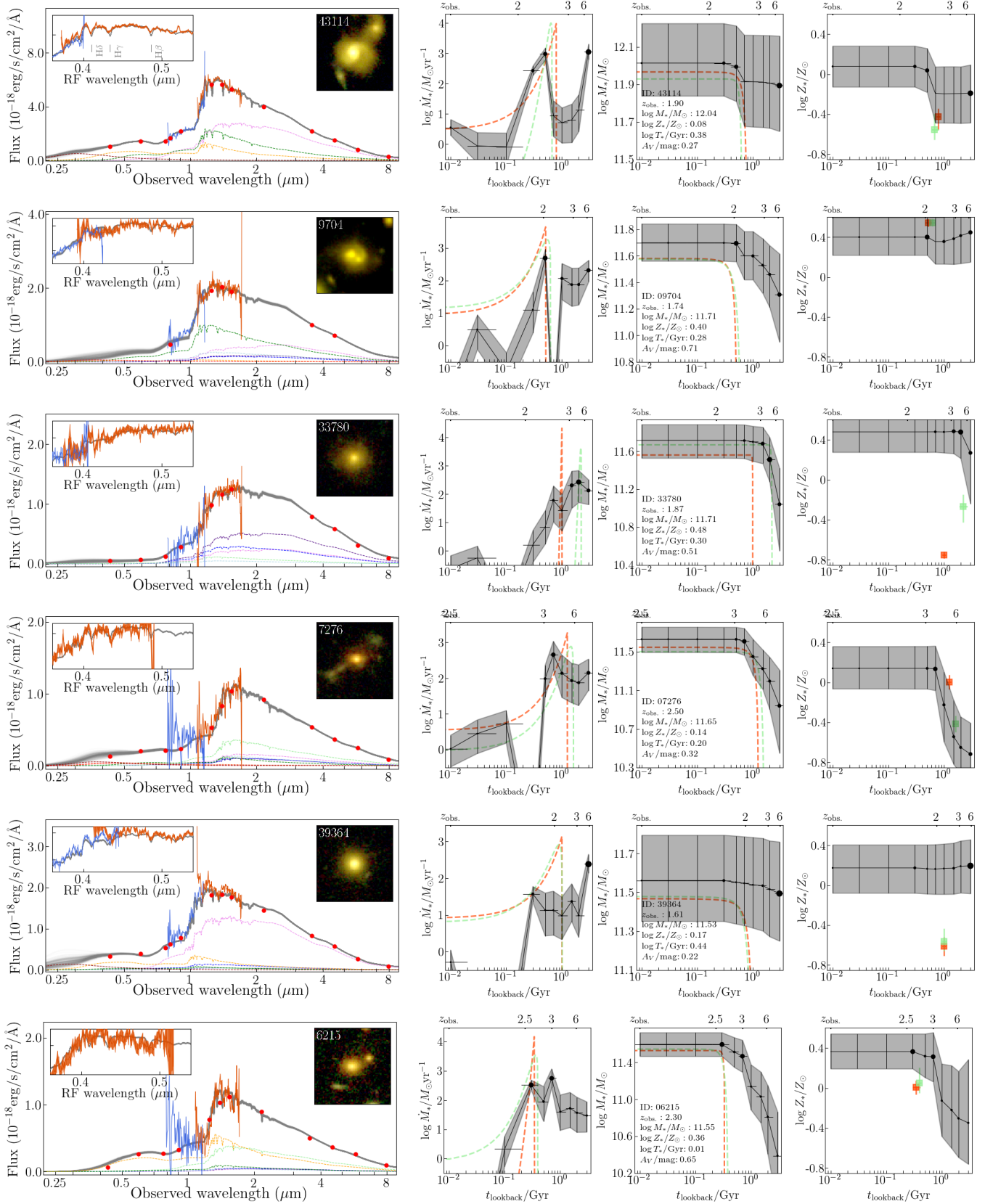


Figure 3. Results of SED fitting for the final 24 galaxies sorted as order of stellar mass. **Left:** Observed spectra (blue and red lines with error bars) for G102 and G141) and photometric data points (red circles with black error bars). Best fit templates of each age bin (dashed lines, colored as in Figure 2) and the sum (gray dashed lines) are shown. Different total templates randomly reproduced from the MCMC chain are also shown. Pseudo color stamps (F160/125/814W for R/G/B; 4.8×4.8 arcsec²) are shown. Emission lines, when detected, are shown with fitted Gaussian curves in the inset (blue solid lines). **Left-Middle:** Reconstructed star formation histories. 50th (black circles) and 16th/84th percentile range is shown (gray hatch region). The size of symbols at each age bin (black circles) represents the amplitude. Best fit star formation histories with functional forms (τ and delayed- τ models) are also shown for comparison (red and green dashed lines). **Right-Middle:** Same as Left-Middle panel, but for stellar mass accumulation histories. **Right:** Same as Left-Middle panel, but for stellar metallicity accumulation histories. The best fit metallicities derived by the two functional models are shown at the best fit age (red/green squares with error bars).

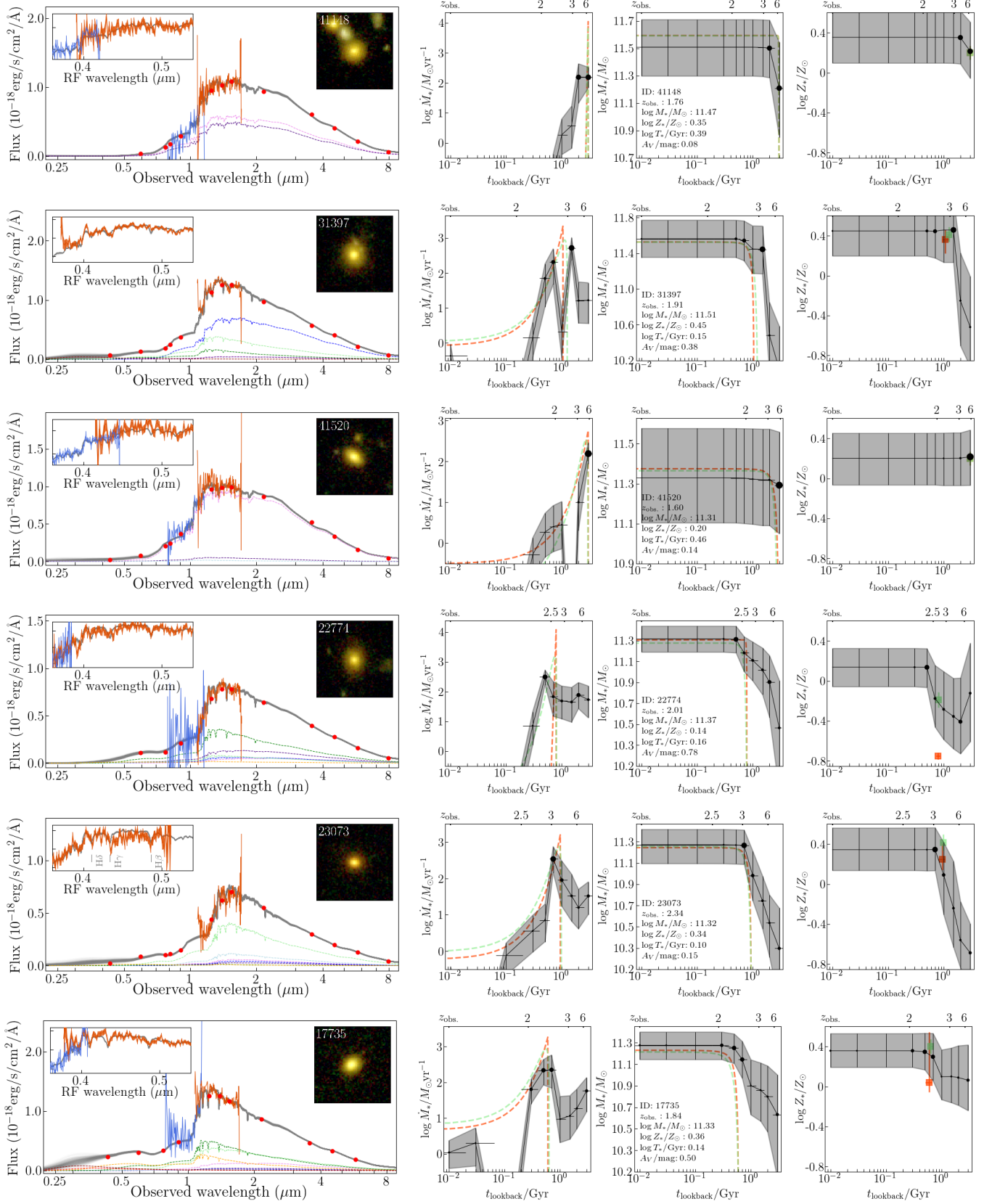


Figure 3. Continued.

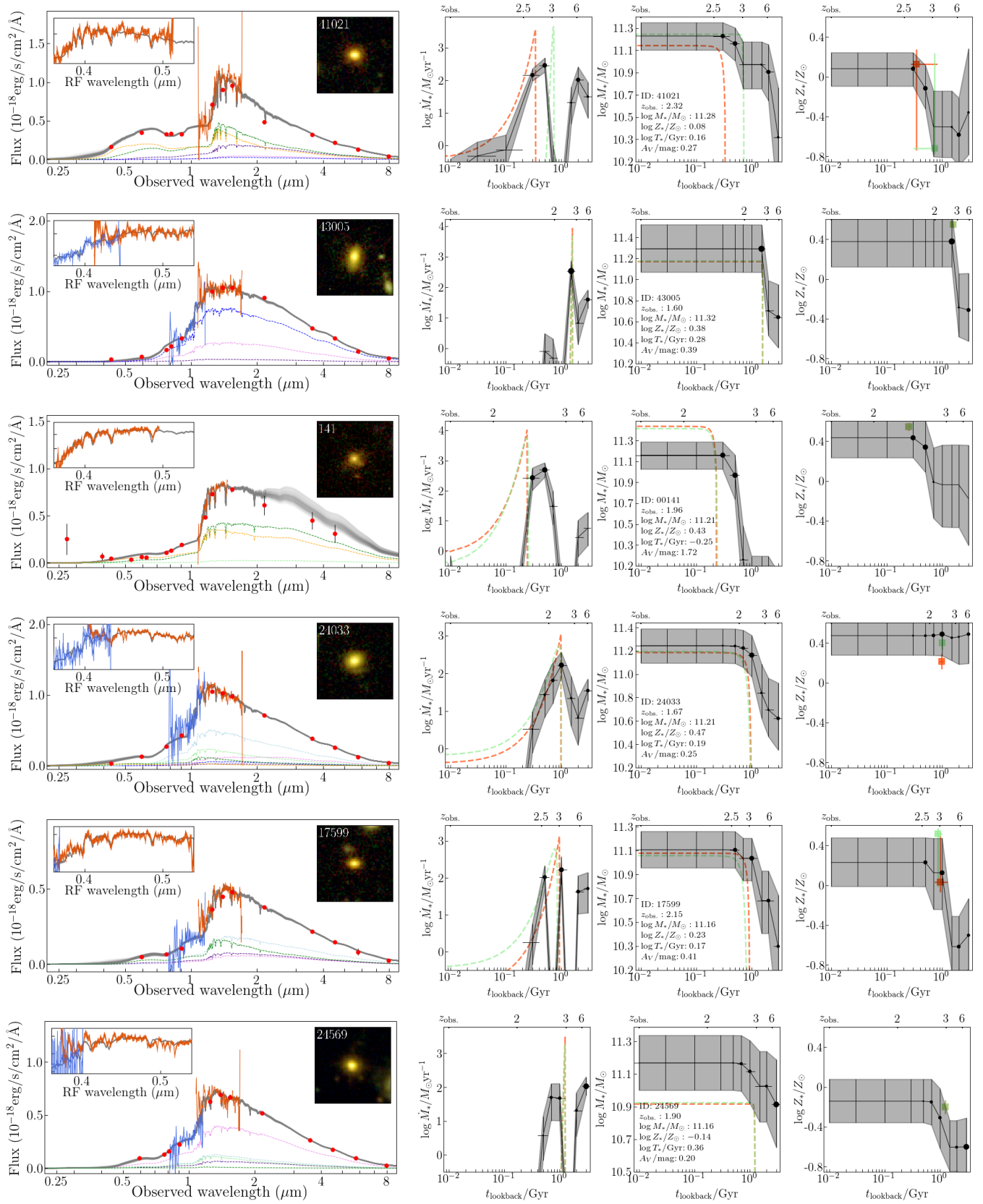


Figure 3. Continued.

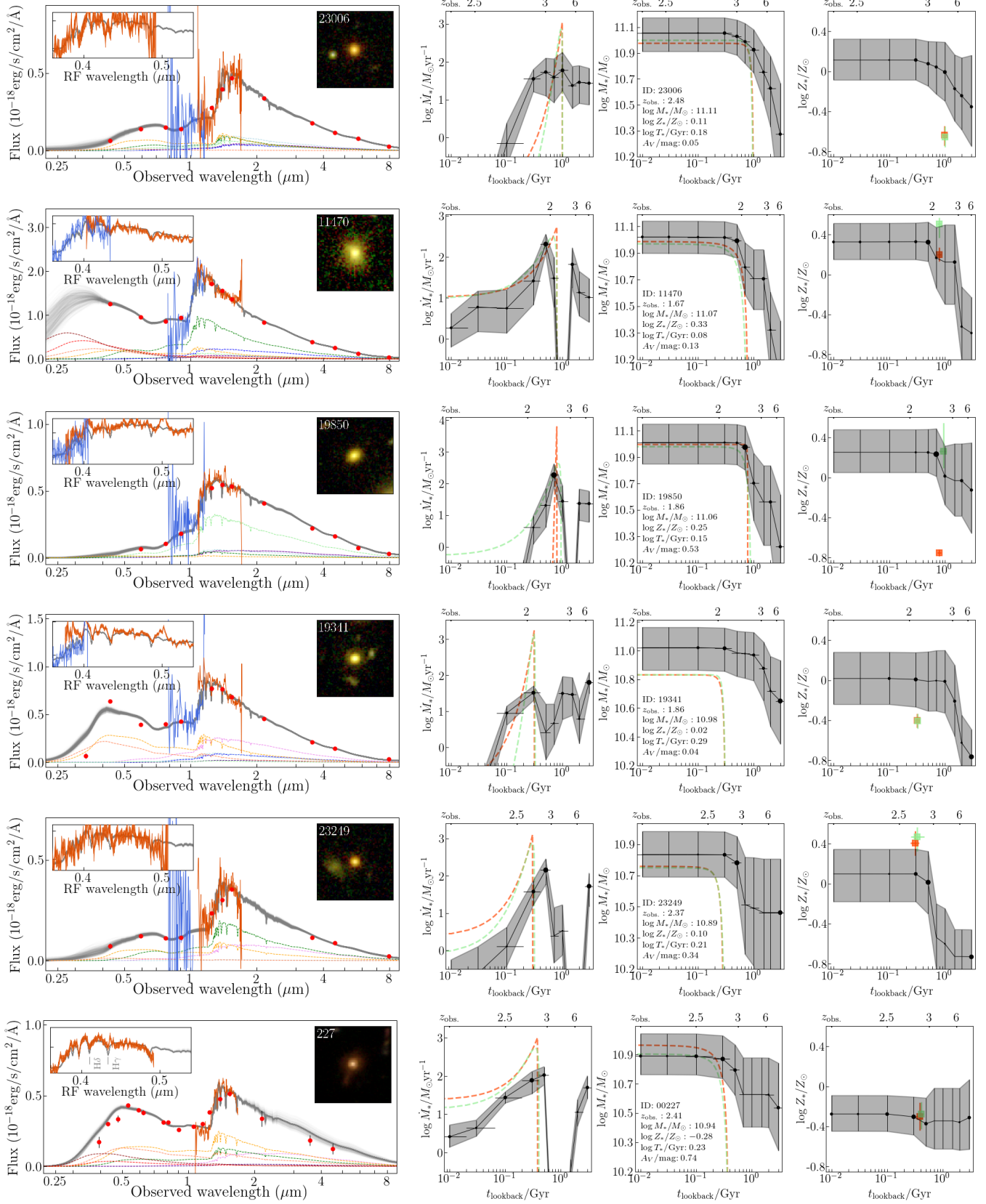


Figure 3. Continued.

the Gaussian fit and the best-fit template as a continuum. For [O II] line, we use relations by Kennicutt (1998) (their Eq.3) to estimate the star formation rates. For H β line, we use assume a recombination coefficient in the Case B (Osterbrock 1989) and then Eq.2 in Kennicutt (1998). These weak emission lines indicate specific star formation rate (SFR/ M_*) of $\lesssim 10^{-10} \text{ yr}^{-1}$. While the detection is tentative, the low level of star formation activity is also observed in previous findings (e.g., Belli et al. 2017), possibly providing more detailed pictures of quenching (see Section 5). Two of emission detected galaxies (IDs 19341 and 19850) have strong [O III] lines (4959 + 5007 Å) with a relatively weak H β line, suggesting existence of AGNs. While H α and [N II] are beyond our wavelength coverage, the line ratio of H β and [O III] lines ($\log \text{H}\beta/[\text{O III}] = 0.15 \pm 0.03$ and 0.13 ± 0.05) implies these galaxies as AGNs in mass-excitation diagram (Juneau et al. 2014).

On the other hand, we find 6 galaxies which consist of very old populations with mass-weighted age $\gtrsim 2$ Gyr, and dominate high-mass end among our sample. While such massive galaxies are rare ($n \sim 3 \times 10^{-5} \text{ Mpc}^{-3}$; Muzzin et al. 2013; Tomczak et al. 2014), it is also true that some of ancient galaxies, that formed a long time ago, have more chance to experience ex-situ processes, e.g., merger and gas accretion, especially at this high redshift. Such ancient galaxies would be smuggled into younger population and become indistinguishable when seen with e.g., light-weighted age. Our reconstructed SFHs have ability to investigate this.

4.3. Reconstructing Star Formation and Metallicity Histories

In the right three panels of Figure 3, we show the reconstructed star formation history (SFH), mass accumulation history, and metallicity enrichment histories for our sample galaxies. We reconstruct star formation rates (SFRs) in each time bin by dividing the amount of stellar mass formed (including the lost mass by the time of observation) by the bin length. Thus, SFRs at each bin represent its average values over the time (~ 30 Myr for the youngest template to ~ 1 Gyr for the oldest one). It is also noted that the derived SFR cannot distinguish between to in-situ (stars formed in the system) or ex-situ (those obtained via mergers).

The total age of each galaxy represents mass-weighted value from the reconstructed SFH,

$$T_* = \sum_i t_i a_i \Psi_i / \sum_i a_i \Psi_i, \quad (1)$$

where t_i is the median age, a_i best-fit amplitude, and Ψ_i mass-to-light ratio of i -th template. An estimated error for each amplitude from the simulation test (Appendix A) is added in quadrature. The typical error in mass-weighted age is ~ 0.2 dex.

Metallicity histories shown in Figure 3 represent mass-weighted accumulated values. Metallicity at j -th age pixel is calculated as

$$Z_j = \sum_{i \leq j} Z_i a_i \Psi_i / \sum_{i \leq j} a_i \Psi_i, \quad (2)$$

where i covers older age pixels than j . Individual metallicity values at each age pixel often suffer from large uncertainty (~ 0.25 dex; Appendix A), while this is partially attributed to small amount of light in those age pixels (i.e. small a_i). We therefore avoid discussing metallicity histories of individual

galaxies, but rather focus on global trend with total metallicity and age in this study (Section 5.4). It is noted, however, that having a parameter for metallicity in each age bin allows flexibility in fitting, and more reasonable estimate (i.e. larger error bars) in star formation histories and SED parameters.

We also fit the same data with functional forms of SFHs to see the agreement. In Figure 3, we show the best fit SFHs obtained with a functional form for the SFH. The same data is fitted in the same manner but with the τ -model, where the SFH is formulated with $\propto A \exp[-(t - t_0)/\tau]$, and one parameter for metallicity. In most cases, the τ -model cannot capture detailed features of SFHs, resulting in larger χ^2/ν than those with gsf (Appendix B; see also recent work by Carnall et al. 2018, who report that functional forms of SFHs cannot reproduce the observed cosmic star formation rate density).

For example, the τ -model cannot capture the dual peaks observed in some galaxies (e.g., 43114). The τ -model also fail to capture extended star formation, both to younger and older sides. This is due to the fact that the functional SFH is light-weighted, where the best fit parameters are more sensitive to differential amounts of light. Such qualitative discrepancy eventually results in quantitative discrepancy in the best fit parameters (Appendix B).

Some galaxies are worth looking in detail. For example, ID43114, the most massive galaxy among our sample ($\log M_*/M_\odot \sim 12$), formed about 50% of the final mass already at $z \gtrsim 5$ (~ 2 Gyr ago). The galaxy was at low star formation activity for ~ 1.5 Gyr, and then started active star formation ($\sim 1000 M_\odot/\text{yr}$) at $z \sim 2.5$, ~ 300 Myr ago. The significant star formation is comparable to those observed as submm galaxies at high redshift (Younger et al. 2007; Tacconi et al. 2008). In fact, its morphology shows a tidal feature with two close objects at the outer part, suggesting a recent (major) merger, consistent with the amount of time to t_{obs} (Lotz et al. 2011; Snyder et al. 2017). Interestingly, the dust attenuation of this galaxy is low ($A_V \sim 0.3$ mag), compared typical SMGs and starburst galaxies at this redshift ($A_V > 3$ mag; Riechers et al. 2013), suggesting a post process has cleared such a large amount of dust.

Other galaxies with obviously disturbed morphology (e.g., IDs 09701 and 00141) also show recent intense star formation at $\lesssim 1$ Gyr before z_{obs} , that may provide independent constraint in merger time scale and induced star formation activity. Those galaxies are thus ideal targets of followup studies of how galaxy quenching occurs in each system.

5. Discussion

5.1. Time scale of star formation

In Figure 4, we summarize the mass accumulation histories as a function of lookback time from the observed redshift. Most of our sample galaxies formed $> 50\%$ of their extant mass by ~ 1.5 Gyr prior to the observation ($z \sim 2.5$ to 5, depending on the observed redshift), which is quantitatively consistent with recent studies at similar and higher redshift (Schreiber et al. 2018; Belli et al. 2018; Estrada-Carpenter et al. 2018).

We estimate the half-mass time, t_{50} (lookback time from the observed redshift), from individual SFHs in the right panel of Figure 4. t_{50} is estimated in each step of MCMC, and thus its uncertainty represents those in SFHs and also individual age bin widths. For some massive galaxies, we only estimate the lower limit, as $> 50\%$ of stellar mass is in the oldest template. Higher resolution spectra by e.g., JWST are required to reveal

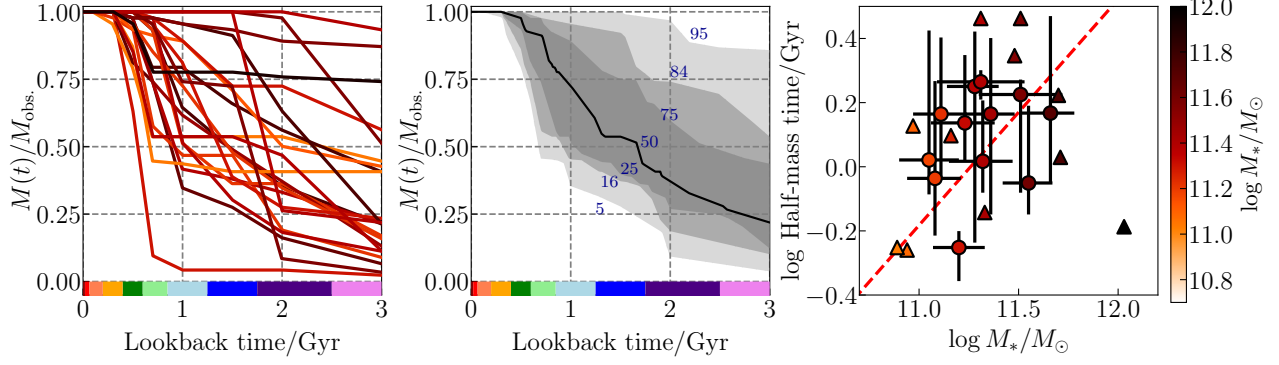


Figure 4. Star formation histories as a function of lookback time from the observed redshift. **Left:** Cumulative stellar mass evolution of individual galaxies. Color corresponds to the final stellar mass. Ages that correspond to the SED templates are indicated with color bars in the bottom (colored as in Figure 2). **Middle:** Summary of individual cumulative stellar mass evolution, where contour boundaries and line correspond to 5/16/25/75/84/95th percentiles and median. **Right:** Half-mass time (lookback time from t_{obs} ; t_{50} in the main text) as a function of observed stellar mass. Those with lower limits are shown with triangles. Symbol color corresponds to the final stellar mass. A positive correlation, $\log t_{50}/\text{Gyr} \propto 0.5 \log M_*/M_\odot$, is seen (red dashed line; i.e. downsizing).

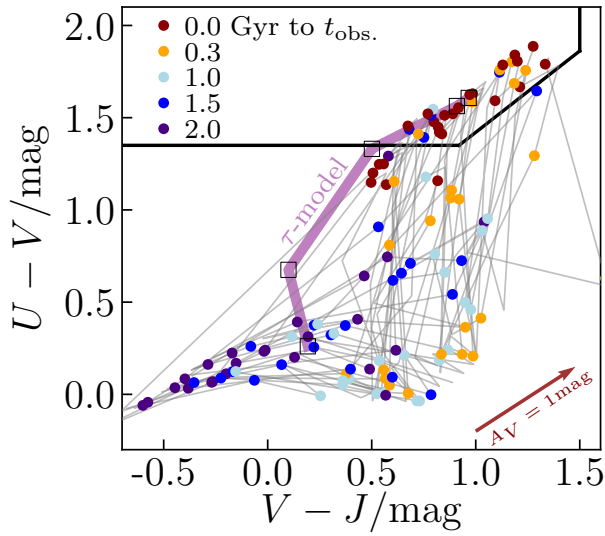


Figure 5. Evolution of rest frame colors of our galaxies in the UVJ diagram, as in Figure 1, to infer the star formation activity/quiescent in the past. Each color at different time is calculated with the derived best fit parameters of each age pixel. We here show the colors at five different times (circles; t_{obs} and [0.3, 1.0, 1.5, 2.0]/Gyr prior to t_{obs}), to avoid a confusing plot. As inferred from individual SFHs (Figure 3) and mass accumulation history (Figure 4), our galaxies spend ~ 1 Gyr, even after having acquired half of their mass (i.e. $t_{50} \gtrsim 1$ Gyr), before entering the quiescent region. Color evolution for a τ -model ($\tau = 0.1$ Gyr; $T_0 = 2$ Gyr) is shown for comparison (purple line; square symbols tag the same past times as for circles) — it enters the quiescent region ~ 1 Gyr after quenching. Reddening by dust attenuation ($A_V = 1 \text{ mag}$) is shown with an arrow at the right bottom.

more ancient histories with a higher time resolution for those galaxies.

We observe a trend where more massive galaxies form earlier, i.e. downsizing (Cowie et al. 1996; Heavens et al. 2004; Treu et al. 2005a), with a linear fit of $\log t_{50}/\text{Gyr} \propto 0.5 \log M_*/M_\odot$. The measured standard deviation (~ 0.16 Gyr) is comparable to the redshift range of our galaxies ($\Delta \log T \sim 0.14$ Gyr). The fact that the downsizing is observed in the early time of the universe hints the galaxy evolution at even earlier epoch when star forming galaxies dominate. While it is possible that our galaxies were once Lyman break galaxies (probably at the bright end) given the observed stellar mass (e.g., Verma et al. 2007), it should be reminded that there is also a population of galaxies that are dusty and missed in most of current optical/NIR observations (e.g., Franco et al.

2018).

5.2. Restframe color evolution

Rest frame colors are also used for discussing the time scale of galaxy star formation (Whitaker et al. 2013; Belli et al. 2018). In Figure 5, we show the evolution of rest frame colors in the UVJ diagram (Williams et al. 2009). We calculate the rest frame colors at each time by summing templates with the best fit parameters. As previously suggested from individual SFHs, most of our galaxies spend a not insignificant amount of time in the star forming region, even after t_{50} . While their star formation activity is low after t_{50} ($\lesssim 10 M_\odot/\text{yr}$ from Figure 3), a large contribution from young/blue templates keeps their UVJ color rather blue until the very end to t_{obs} .

On the other hand, there are a few galaxies that stopped star formation rapidly (whose color evolution partially overlapping with τ -model). For example, ID43005 (one with green/orange points near the boundary in Figure 5) has formed most of their stars $\gtrsim 1.5$ Gyr ago, though our method has a lower time resolution and we cannot conclude if there were any quenching processes.

Belli et al. (2018) recently present a similar result, where they refer to the former and latter evolution tracks as “slow” and “fast” quenching paths respectively. A question to be pursued is what physical conditions make galaxies choose either track (see, e.g., Lilly & Carollo 2016; Whitaker et al. 2017; Abramson & Morishita 2018). We follow this argument in Paper II in combination with their structural parameters.

It is also worth noting that there are several galaxies that fall in the quiescent region *before* t_{50} — those with blue/dark blue dots inside the quiescent boundary in Figure 5. These galaxies are characterized by dual peak SFHs, implying that they might evolve on the “fast quenching” track but later star formation activity (induced by, e.g., merger) forces their colors back to the star forming region (as seen for ID43114).

5.3. Stellar Mass-Metallicity Relation at $z \sim 2$

The stellar mass-metallicity relation is a key diagnostic of galaxies’ chemical and mass maturation histories. The relation encodes the coevolution of stellar mass and chemical enrichment among galaxies, and provides an independent clue to the past evolution than star formation histories. The relation is known to hold from the local universe (Gallazzi et al. 2005; Panter et al. 2008; González Delgado et al. 2014), in a wide range of mass (Kirby et al. 2013), up to $z \sim 1$ (Gallazzi

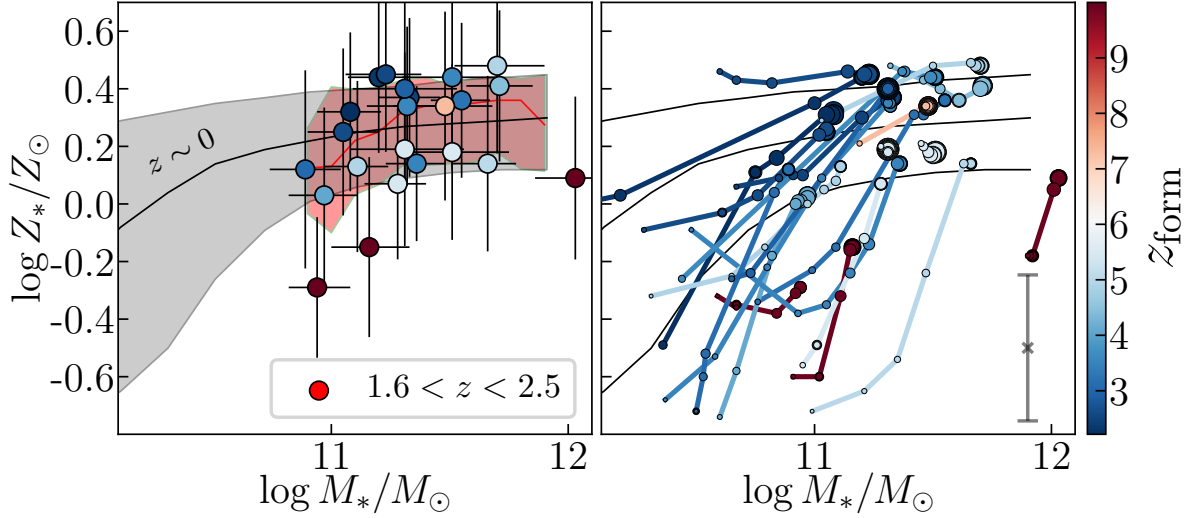


Figure 6. **Left:** Stellar mass-metallicity relation of 24 galaxies in this study (circles). The symbols are color-coded by formation redshift, z_{form} . Running median (~ 0.25) is shown with 16-84th percentile range (red line with hatched region; $\sigma_{\log Z} \sim 0.15$). Most of our galaxies at $z \sim 2$ already have consistent values to the local metallicity value (gray hatched region represents 16-84th percentile range from Gallazzi et al. 2005, with a calibration shift for +0.15 dex; Section 5.3). **Right:** Same as left panel, but metallicity enrichment histories for individual galaxies (right panel of Figure 3). The symbol size represents different time bins (small to large for $t = -3$ Gyr to 0 from t_{obs}). Typical uncertainty at each age pixel (~ 0.25 dex) is shown at right bottom.

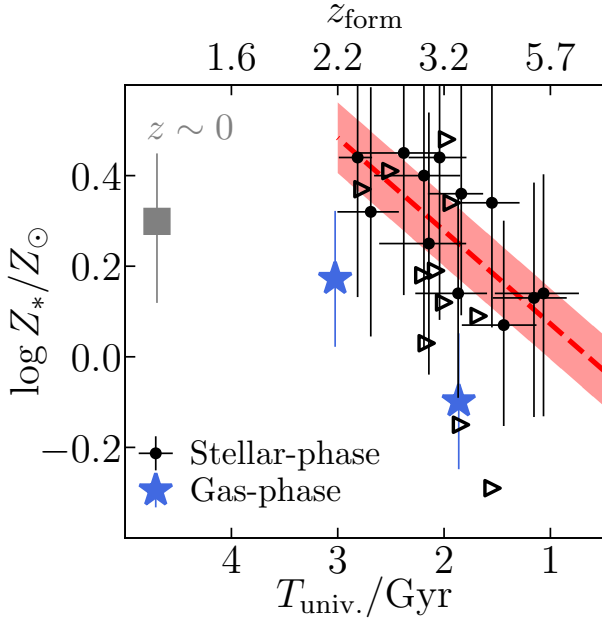


Figure 7. Observed stellar metallicity as a function of the formation time, or z_{form} (black circles/triangles for those with an upper limit in age estimate). The linear fit with a slope (0.20 ± 0.08 dex/Gyr) and standard deviation ($\sigma \sim 0.16$ dex) is shown (red dashed line and hatched region). The local metallicity value of the most massive galaxies ($\log M_*/M_\odot \sim 11.5$; Gallazzi et al. 2005) is shown for comparison (gray square). Gas phase metallicity measurements of massive galaxies ($\log M_*/M_\odot = 11.5$) at similar redshifts (Maiolino et al. 2008) are shown (blue stars), after calibrated to the local Z_* measurement (Section 5.3).

et al. 2014; Choi et al. 2014; Leethochawalit et al. 2018). Beyond the redshift, however, it is still studied with small sample galaxies and not clear (Onodera et al. 2012; Onodera et al. 2015; Kriek et al. 2016; Morishita et al. 2018). While the relation in gas-phase metallicity at $z \gtrsim 1$ may suggest the relation may remain universal to higher redshift (Tremonti et al. 2004; Mannucci et al. 2010; Kewley & Ellison 2008; Maiolino et al. 2008; Yabe et al. 2014; Zahid et al. 2014; Onodera et al. 2016;

Wang et al. 2017), the observed scatter is still large, due to both a selection bias, different tracer of metallicity, and different physical state of gas phase metallicity (e.g., Andrews & Martini 2013). We here for the first time overview the relation at $z > 1.6$.

In the left panel of Figure 6, we show the stellar mass-metallicity distribution of our galaxies at the observing redshift. The metallicity is mass-weighted as the age (Equation 1). No significant mass dependency of the metallicity is observed, as our galaxies occupy the high-mass end and do not span a wide dynamic range. This a flattening behavior is consistent with relations at lower redshift (Gallazzi et al. 2005, 2014).

The past trajectory can be followed by the reconstructed metallicity histories, shown in the right panel of Figure 6. In contrast to what is found in the left plot (mass-independence), we see evolution of metallicity as a function of mass for each system. It is noted, however, that age-metallicity degeneracy could also reproduce this trend, where old templates are biased to lower metallicity and vice versa. Given this systematic uncertainty, and the fact that uncertainty in metallicity at each age pixel remains nonnegligible (~ 0.25 dex from our mock test) for most of our galaxies, we leave this conclusion pending in this study.

To compare with the local relation derived in Gallazzi et al. (2005), we need a calibration of the absolute value of metallicity. While Gallazzi et al. (2005)'s metallicity measurement is based on the total metallicity, as in this study (as opposed to each element abundance), there is a systematic difference due to adopted isochrones (MIST vs. Padova), each of which has a different definition of solar metallicity ($Z_\odot = 0.0142$ vs. 0.0190). We correct this by applying +0.15 dex offset to the Gallazzi et al. (2005)'s metallicity measurement. After the calibration, we find that most of our galaxies are already on the local relation, with median of $\log Z_*/Z_\odot \sim 0.25$, and the scatter around the median similarly small as the local one (~ 0.15 dex).

While we discuss the scientific aspect of this in Section 5.4, it is worth noting possible systematics. Due to the low-

resolution spectral data set, it is not clear if these metallicity is enhanced by α -elements, despite its completely different origin from iron (e.g., Thomas et al. 2005). In fact, Leethochawalit et al. (2018) recently found that ~ 0.16 dex decrease in iron abundance of massive galaxies at $z \sim 0.4$ compared to the local value. Given the time of universe (when iron was relatively deficient) and short time scale of star formation for our galaxies (where α -elements are enhanced), the high $\log Z_*/Z_\odot$ values may represent the α enhancement, as is the case for $z \gtrsim 1$ galaxy (Onodera et al. 2015; Kriek et al. 2016), though it requires higher resolution spectra to infer detailed element abundances.

Two galaxies fall below the median relation (IDs 00227 and 24569). The former galaxy, which was reported and discussed in Morishita et al. (2018), shows rather extended star formation histories with small metallicity values over the entire history. According to its undisturbed morphology and gradual mass increase seen in its history, accretion of low mass satellites (i.e. with low metallicity) or late time star formation triggered by the infall of metal poor gas may explain the observed properties, rather than more dramatic episode involving, e.g., major merger. Detailed look of its inner structure at a higher angular resolution would provide further insight into its chemical evolution (e.g., Abramson et al. 2018; Wang et al. 2018).

The other galaxy, on the other hand, shows a rapid assembly of mass in the early time, $z \gtrsim 6$. Since the galaxy formed $\sim 90\%$ of its current mass by the time, its low metallicity is consistent with the cosmic metal enrichment (e.g., Lehner et al. 2016) as well as an observed rapid decrease in gas phase metallicity at a given mass (Troncoso et al. 2014; Onodera et al. 2016). Given the time left to $z \sim 0$, this kind of galaxies would possibly be enriched in metallicity by, e.g., mergers and recycled gas, and may sneak into the local average population (see discussion in Morishita et al. 2018). Those rare galaxies would be thus ideal followup targets for investigating possible remnants of the first/second generation stars, akin to one reported in Kriek et al. (2016).

5.4. Metallicity Enrichment Histories

While the mass-metallicity relation indicates that our galaxies are already enriched to the value at present day (Figure 6), its origin and observed scatter is yet to be investigated. We investigate global properties by considering the formation time (z_{form}), which is derived with the mass weighted age and observed redshift, $T(z_{\text{form}}) = T(z_{\text{obs}}) - T_*$. We show the distribution in Figure 7. A clear correlation between T_{form} and observed metallicity is observed, where the linear fit reveals a slope of $\log Z_*/dt \sim 0.20 \pm 0.08$ dex/Gyr, with a standard deviation of ~ 0.15 dex.

Previous studies suggest that the most massive galaxies ($\log M_*/M_\odot \gtrsim 11.5$) have already enriched the metallicity to the local value at $z \sim 2$ (e.g., Panter et al. 2008) but little is said beyond the time. This is mainly due to the fact that the time accessible from the local universe is limited to $z \lesssim 2$ ($\lesssim 10$ Gyr) with a medium resolution spectrum. Our result shows the metallicity enrichment happening in this class of massive galaxies for the first time, whose metallicity already reaches the local value at $z \sim 3$.

One may suspect this is an artifact from the age-metallicity degeneracy. While some galaxies show a weak correlation between the two parameter, the range is small, and also smaller than quoted error bars in Figure 7. Our simulation test also revealed that the total metallicity/age are reproduced reliably enough for the observe trend (see Appendix A).

Interestingly, the linear fit suggests that the metallicity even exceeds the local value of the most massive galaxies in Galazzi et al. (2005) by ~ 0.1 dex. As noted before, our sample galaxies are biased to compact, high density galaxies at the similar redshift. While compact massive galaxies is rare at $z \sim 0$ (Taylor et al. 2010, but see also Poggianti et al. 2013), the later evolution in the following ~ 10 Gyr of our galaxies would possibly resolve the tension. We discuss this in the following section.

In Figure 7, we also plot the gas-phase metallicity measurements of star forming galaxies in the similar redshift range for comparison. We use the formula derived in Maiolino et al. (2008) at the same mass ($\log M_*/M_\odot = 11.5$), with calibration by matching stellar and gas phase metallicity measurements at $z \sim 0$. While matching two different metallicity is challenging and doing so in this way is not necessarily motivated by any physical reasons, this suffices our purpose here, i.e. comparison of the *relative* difference at high redshift.

While keeping this in mind, it is interesting to find an offset of ~ 0.2 - 0.3 dex between those metallicity measurements in our redshift range, that may give us a clue to how those galaxies enriched metallicity. Assuming those star forming galaxies are star forming counterparts of our passive galaxies, the gap should be resolved during the time when they stop the forming stars and when they are observed as passive galaxies.

The gap may be attributed to the dilution of gas-phase metallicity by infalling pristine gas. If this is the case, it is suggested that galaxy quenching may be largely caused by termination of gas infall (e.g., Feldmann & Mayer 2015).

Another possible explanation is a low-level star formation activity in a closed box, or “strangulation” (Larson et al. 1980; Peng et al. 2015). Peng et al. (2015) demonstrated this by using chemical evolution models for massive star forming and passive galaxies in the local universe, that show an offset of ~ 0.1 dex in metallicities. Rapid cessation of star formation, such as AGN and stellar feedback, would rather reproduce a similar metallicity for the two populations. Recent observations revealed low-level star formation activity (e.g., Gobat et al. 2017; Belli et al. 2017) and gas content (Gobat et al. 2018) in massive quiescent galaxies at the similar redshift. This closed-box evolution would be in a good agreement with what we see in individual star formation histories (Figure 3), which independently supports our speculation here. We revisit this in combination with structural evolutionary influences in Paper II.

5.5. Following Evolution to $z \sim 0$

We have found that our galaxies are already enriched in metallicity, located on, or even above, the local mass-metallicity relation. Given the amount of mass and its quiescence, it is of our interest to investigate how these galaxies will evolve to the local population. While there is a large uncertainty to expect their descendant (as described in Introduction), it is still worth describing their possible paths and mechanisms.

First thing to note is that our sample galaxies are on average compact, high density galaxies ($\langle r_{\text{eff}} \rangle \sim 2$ kpc; possibly due to the selection bias toward high spectral S/Ns), as found at similar redshifts. Compact galaxies at these redshifts are often debated in terms of size evolution, where observed size is ~ 3 - 5 smaller than galaxies at $z \sim 0$ with similar masses (Trujillo et al. 2007; van der Wel et al. 2014; Morishita et al. 2014). While it is still under much debate if (all of) these galaxies need to follow such a significant size evolution (Nipoti et al.

2012; Newman et al. 2012; Poggianti et al. 2013; Belli et al. 2017), minor merger is a popular mechanism that can efficiently increase their sizes (e.g., Naab et al. 2009; Hopkins et al. 2009; Oser et al. 2010; van Dokkum et al. 2015; Morishita & Ichikawa 2016).

The scenario appears to consistently work for our result of metallicity, where accretion of low-mass galaxies (which are less-metal enriched; cf. mass metallicity relation) would dilute the system’s metallicity to the consistent value. For example, ~ 5 minor mergers (with 1/10 mass of the host, and metallicity inferred from the relation at $z \sim 2$) would lower the host metallicity by ~ 0.1 dex, being consistent with the local value. The metallicity gradient observed in the local universe (e.g., González Delgado et al. 2014; Martín-Navarro et al. 2018) is independent evidence that such high- z metal-rich galaxies would become cores while the accreted component locates the outer part of local massive galaxies. The integrated metallicity is rather an average value of the whole system, and thus metallicities observed in the local relation should be lower than those observed at higher redshifts.

Infall of metal poor gas associated with minor merging satellites (e.g., Torrey et al. 2012) or direct infall from the cosmic web (Dekel & Birnboim 2006) would also dilute the system’s total metallicity by inducing the second burst. While this scenario is unlikely to reproduce the observed metallicity gradient, there is a large fraction of early-type that show an evidence of on-going star formation (e.g., Treu et al. 2005b; Kaviraj et al. 2011). Detail studies of metallicity of intermediate galaxies will shed light on how these different scenarios contribute to the evolution path of massive galaxies at high redshift to the local counterpart.

6. Summary

We reconstructed formation histories of 24 massive, passively evolving galaxies at $z \sim 2$. Our new SED modeling simultaneously fit slitless spectroscopic and photometric data taken from multiple surveys, with no functional assumption for star formation histories. Our main findings are as follows.

1. Our massive galaxies have already formed $> 50\%$ of their current mass by ~ 1.5 Gyr prior to the epoch of observation, with a downsizing trend that more massive galaxies evolve earlier.
2. Star formation histories reconstructed by our new SED modeling show more extended feature than what are expected with a τ -model fitting for most of the sample galaxies, indicating a low-level star formation activity until recently, rather a than abrupt cessation.
3. Stellar-phase metallicities of most of our galaxies are already compatible with, or even higher than, local values, indicating a rapid metallicity enrichment being associated with the early stellar mass formation.
4. By using the reconstructed star formation histories and inferred metallicity, we revealed a rapid metallicity enrichment of this class of massive galaxies, at a rate of ~ 0.2 dex/Gyr in $\log Z_*/Z_\odot$ from $z \sim 5.5$ to $z \sim 2.2$.
5. The observed gap between the stellar phase metallicity and gas phase metallicity can be explained by dilution of gas-phase metallicity due to the inflow of pristine gas to star forming galaxies and/or continuation of low-level of star formation in quiescent systems. The latter scenario provides a picture where galaxy quenching

happens more smoothly, rather than abrupt/rapid termination, consistently but independently confirming our findings of individual star formation histories.

Software: Astropy (Muna et al. 2016), *emcee* (Foreman-Mackey et al. 2013), *lmfit* (Newville et al. 2017), *Grizli* (Brammer 2018), *python-fsps* (Conroy et al. 2009; Conroy & Gunn 2010; Foreman-Mackey et al. 2014)

We thank anonymous referee for reading the manuscript carefully and providing constructive comments. We thank Marco Chiaberge, Colin Norman, Benedikt Diemer, Kartheik Iyer, Sara Ellison, and Susan Kassin for fruitful discussion. We thank Pascal Oesch for providing their HDUV data prior to the public release. Support for GLASS (HST-GO-13459) was provided by NASA through a grant from the Space Telescope Science Institute, which is operated by the Association of Universities for Research in Astronomy, Inc., under NASA contract NAS 5-26555. Support for this work is provided by NASA through a Spitzer award issued by JPL/Caltech, HST-AR-13235 and HST-GO-13177. MT acknowledges the support provided by the Australian Research Council Centre of Excellence for All Sky Astrophysics in 3 Dimensions (ASTRO 3D), through project number CE170100013.

Appendix

Appendix A: Mock Simulation of SED Fitting

We test the fidelity of galaxy SFHs and other parameters by our SED fitting method.

A1: Simulation Setup

To explore parameter spaces we are interested in this study (i.e. quenched galaxies at $z \sim 2$), we set parameters as follow; redshift $z \in [1.6 : 2.5]$; mass-weighted age $T_*/\text{Gyr} \in [0.6 : 2.2]$ peaked at ~ 1.5 Gyr; dust attenuation $A_V/\text{mag} \in [0 : 2.5]$ with a flat distribution; metallicity $\log Z_*/Z_\odot \in [-0.5 : 0.5]$, peaked at $\log Z_*/Z_\odot = 0.15$ dex (top panels of Figure 8). Amplitudes of each template (a_i ; i.e. SFHs) are randomly assigned.

The mock spectra and photometry are generated via FSPPS (Conroy et al. 2009; Conroy & Gunn 2010) with the assigned parameters. Broadband photometry is also simulated by convolving the mock template with filter response curves and add the observed noise. For grism spectra, we convolve the mock template with observed line spread function (modeled with a gaussian), which takes account of morphology/instrumental convolution. Error of each spectral element and broadband photometry is given within the uncertainty of observed data, randomly taken from 24 galaxies in this study ($\sim 5\text{-}20/\text{pixel}$ at $3700 < \lambda_{\text{rest}}/\text{\AA} < 4200$; Table 1).

No emission lines are added since our focus is the quenched/old galaxy population. In total 600 mock sets of G102/G141 spectra+brodband photometry are prepared from the template generated with random sets of parameters. We follow the same fitting method as in the main text.

A2: Result of Global Parameters

Figure 8 shows the offset of output and input values ($\Delta y = y_{\text{out}} - y_{\text{in}}$) as a function of output value for major parameters—stellar mass, mass-weighted age, dust attenuation, and metallicity of the mock galaxies. By taking output values (rather than input ones) in x -axis, it is possible to infer the false-positive fraction at a given output (i.e. observed)

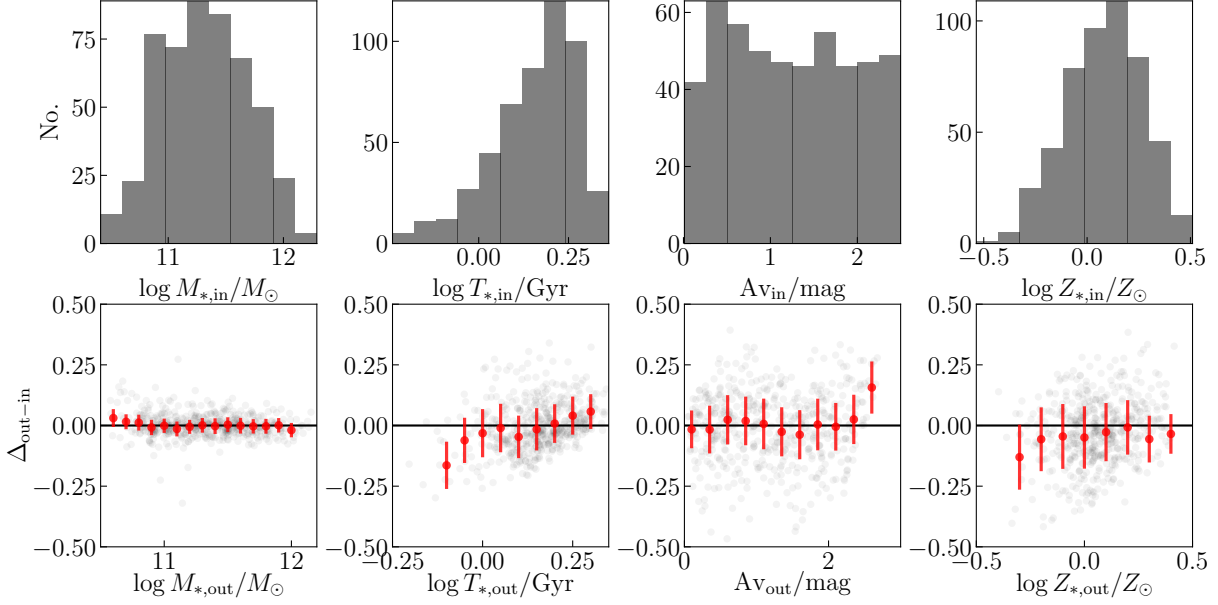


Figure 8. **Top:** Parameter distributions of 600 mock galaxies. Noted that age is distributed in a linear scale (peaked at ~ 1.5 Gyr), but shown in a log scale here. **Bottom:** offsets of input and output values ($\Delta_{\text{out-in}}$; solid lines represent zero point). Median offsets and 16/84th percentiles range at each output bin are shown (red circles and error bars). Stellar mass, dust attenuation, and mass-weighted metallicity show good agreement for the parameter ranges of our galaxies. While a weak positive correlation is seen in mass-weighted age, the measurement is not biased and scatters are small ($\sigma \sim 0.1$) at the median value of our sample ($\log T_*/\text{Gyr} \sim 0.2$).

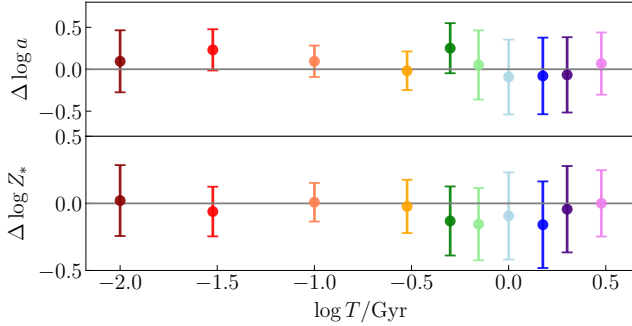


Figure 9. Mean offsets for amplitude ($\log a_{i,\text{out}} - \log a_{i,\text{in}}$; top panels) and metallicity ($\log Z_{i,\text{out}} - \log Z_{i,\text{in}}$; bottom panels) with standard deviation at each age pixel from the mock test. The measured standard deviation is added in quadrature to observed uncertainty (i.e. star formation and metallicity histories).

value, and also implement the scatter to observed values for more comprehensive estimate of uncertainty.

We find excellent agreement in stellar mass with scatter of ~ 0.05 dex, and moderate agreement in mass-weighted age, dust attenuation, and mass-weighted metallicity with scatters of ~ 0.11 , 0.14 , and 0.13 around median values. Median offsets are small for most of parameter ranges. Mass-weighted age shows a negative slope, underestimating for ~ 0.15 dex at $\log T \lesssim -0.05$. However, most of our sample galaxies dominate higher values, with a median of $\log T_*/\text{Gyr} \sim 0.2$ (Figure 4), where the bias in parameters is small, and thus we do not correct the offset for our galaxies in the main text.

A3: Result of SFHs

In Figure 9, we summarize offsets of output and input values for amplitude and metallicity at each age pixel to show the fidelity of SFHs and metallicity enrichment histories from all mock galaxies used here. While the offset and scatter may depend on parameter sets with different combinations, this suggests that SFHs can be determined in ~ 0.5 dex accuracy.

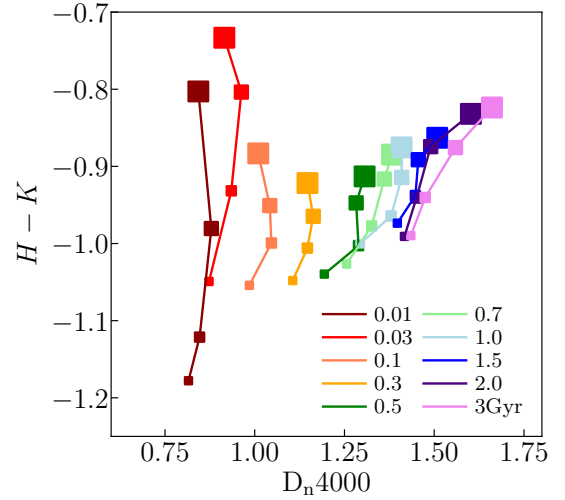


Figure 10. Rest frame NIR color ($H-K$) as a function of strength of 4000 \AA (D_{n4000}), for each age (lines with different colors) and metallicity ($\log Z_*/Z_\odot = -0.8, -0.4, 0, 0.4$ for small to large symbols). Both parameters are derived from templates which are convolved to a comparable resolution of retrieved grism data ($R \sim 150$), though this is minimal effect here. Age and metallicity are nearly orthogonal in most of the parameter space, except for old and solar/super-solar metallicity population at the right top.

Metallicity shows a large scatter in reproduced values, with standard deviation of ~ 0.3 dex. Given the parameter range assigned for metallicity ($\in [-0.8 : 0.6]$), we conclude that determination of metallicity at each age pixel is challenging with the current data set. It is noted that this does not mean that reproduced *total* metallicity has comparable uncertainty, since part of the scatter can be attributed to the age pixel where the total contribution of light is small. Total metallicity, which is light or mass-weighted, should remain less scattered ($\lesssim 0.2$ dex), as shown in the main text and A2.

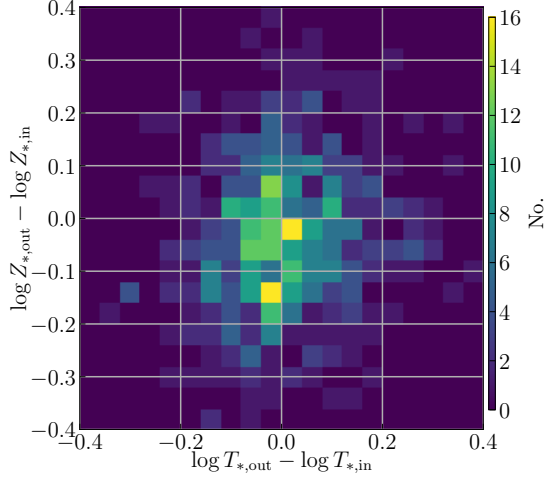


Figure 11. Distribution of offset of age ($\log T_{*,\text{out}} - \log T_{*,\text{in}}$; x-axis) and metallicity ($\log Z_{*,\text{out}} - \log Z_{*,\text{in}}$; y-axis) from our mock test. Color represents the number of galaxies in each grid. The distribution is almost symmetric around the zero point, whereas it would follow a negative slope in case of the age-metallicity degeneracy.

A4: Age-Metallicity Degeneracy

Degeneracy between age and metallicity is notoriously known as one of difficult aspects when modeling accurate SEDs from photometric data (Worthey 1994). The degeneracy is however resolved once one obtains both information at optical and NIR wavelength range simultaneously (de Jong 1996; Smail et al. 2001), where the former light is dominated by the main sequence stars while the latter by AGB stars (as seen in Figure 2; also Choi et al. 2016, for more details).

To see if this is the case for our data set, we first show in Figure 10 a rest frame NIR color- D_n4000 diagram, both of which are available with our data in this study. Rest frame NIR color ($H - K$) and the strength of 4000 Å (D_n4000 Balogh et al. 1999) are calculated with templates used for fitting, which are convolved to a comparable resolution of grism data ($R \sim 150$), including the convolution effect by source morphology. As we see in the figure, age and metallicity are nearly orthogonal in most of the parameter range, meaning the age and metallicity can be well separated from those measurement. The only exception is for old ($\gtrsim 1.5$ Gyr) and solar/super-solar metallicity, where the relation of the two measurements becomes less orthogonal. Due to this, metallicities of our fitting typically have larger uncertainties for old populations.

We also investigate the age-metallicity degeneracy with our mock data set. In Figure 11, we show the distribution of offset in total mass-weighted age and metallicity for our mock galaxies. The distribution is symmetric in both axes, whereas the distribution would follow a negative slope if these parameters are degenerated. The distribution is scattered for ~ 0.2 dex, which is consistent with those found in A2.

From both tests here, we conclude that the data set used in this study can resolve the age-metallicity degeneracy for our moderately old galaxies ($\lesssim 2$ Gyr), but star formation and metallicity histories become less certain beyond $T_{\text{lookback}} \gtrsim 2$ Gyr.

Appendix B: Comparison of SED parameters obtained with functional SFHs

In Section 4.3, we see that our reconstructed SFHs capture the detail features of individual galaxy SFHs, that are often

missed with functional forms. While the deviation is clear in these comparison, it is yet to be investigate how different assumption of SFH results in SED parameters. We here compare the best fit parameters between two types of SFHs.

In Figure 12, we compare the goodness of fit, χ^2/ν , and major parameters from SED fitting, i.e. stellar mass, *light-weighted* age and metallicity, and dust attenuation. These values are compared between those reproduced by *gsf* (main text) and functional ones. Firstly, the goodness of fit is better with *gsf* for most of our galaxies, which is reasonable given the flexibility of its modeling. We also find that the τ -model ($\propto \exp[-t/\tau]$) is more sensitive to the light from young stellar populations, where the model systematically underestimates system's ages for ~ 0.3 Gyr on average (top panels). The discrepancy propagates to other parameters, where we find over estimated dust attenuation (~ 0.3 mag) and largely underestimated metallicity.

The discrepancy in age and dust becomes slightly smaller when the delayed- τ model ($\propto t \exp[-t/\tau]$) is used (bottom panels of Figure 12). This is shown in the goodness of fit, where the delayed- τ model results in smaller values of χ^2/ν (see also Pacifici et al. 2016). This is partly attributed to its rising slope in SFHs, which makes the age slightly older and cancel out discrepancy in other parameters. A large discrepancy in metallicity, however, still remains.

Despite this, it is interesting that the reproduced stellar mass is very consistent with each other, with only ~ 0.1 dex scatter in $\log M_*$ among our sample. While it is challenging to comprehensively understand this agreement due to a large number of parameters here, this is partly due to the sufficient wavelength coverage to the rest-frame near-IR region, where the light from low-mass stars dominates and less sensitive to other parameters (e.g., Bell et al. 2003). The contribution by other parameters (i.e. age/metallicity/dust) are cancelled out due to partial degeneracy at a given form of star formation history. However, this does not necessarily means that the typical error in stellar mass remains comparably small. As shown in the main text and Appendix A, the stellar mass measurement with *gsf* accompanies with ~ 0.2 dex uncertainty, that is mainly originated from, e.g., systematics in estimating accurate star formation and metallicity enrichment histories. (And therefore the estimated uncertainty in stellar mass with functional form SFHs are much smaller here.) For this reason, we conclude that stellar mass measurement remains, at least, ~ 0.15 dex accuracy for our galaxies, and possibly for other types of galaxies, since the uncertainty comes from its assumption of SFHs and SED modeling. The best fit parameters derived with the two functional SFHs are summarized in Table 2.

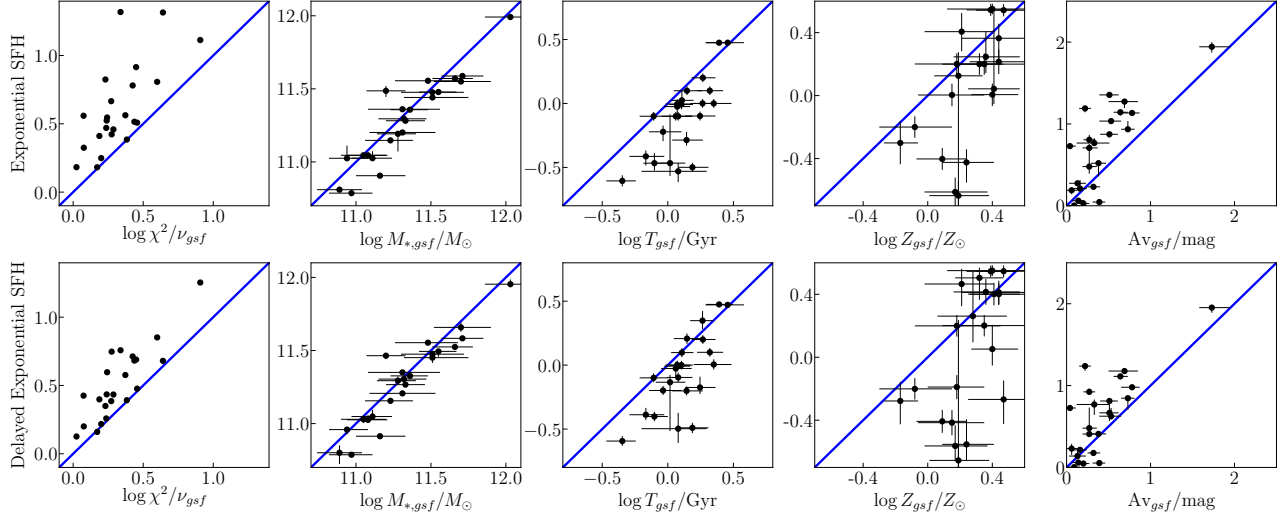


Figure 12. Comparison of χ^2/ν , and SED parameters for 24 galaxies in this study derived from different SFHs, with gsf (x-axis) and with functional forms for SFHs (y-axis). Exponential model (top) and delayed model (bottom) are examined. The goodness of fit is better with gsf for most of our sample. While both SFHs reproduce the stellar mass in a good agreement, the functional SFHs overestimate dust attenuation and underestimate age and metallicity. It is noted that age and metallicity of gsf are light-weighted values to match those derived with functional form SFHs, while those in the main text are mass-weighted values.

Table 1
Summary of physical parameters.

Obj ID	RA (degree)	Dec (degree)	z_{grism}	$\log M_*$ (M_\odot)	$\log Z_*$ (Z_\odot) ^c	$\log T_*$ (Gyr)	A_V (mag)	$U - V$ (mag)	$V - J$ (mag)	S/N ^a blue red	t_{G102} ^b (sec)	t_{G141} ^b (sec)
MACS J1149.6+2223 ^d												
00141	1.77403e+02	2.24185e+01	1.96 ^{+0.01} _{-0.01}	11.20 ^{+0.13} _{-0.13}	0.44 ^{+0.17} _{-0.17}	-0.26 ^{+0.12} _{-0.13}	1.73 ^{+0.22} _{-0.15}	1.79 ^{+0.01} _{-0.01}	1.35 ^{+0.10} _{-0.07}	4.2 24.5	9529	75987
00227	1.77407e+02	2.24162e+01	2.41 ^{+0.01} _{-0.01}	10.94 ^{+0.14} _{-0.12}	-0.29 ^{+0.18} _{-0.14}	0.24 ^{+0.12} _{-0.13}	0.73 ^{+0.08} _{-0.08}	1.20 ^{+0.01} _{-0.01}	0.81 ^{+0.00} _{-0.05}	6.8 17.4	19758	80399
GOODS-North												
06215	1.89029e+02	6.21726e+01	2.30 ^{+0.02} _{-0.02}	11.55 ^{+0.12} _{-0.13}	0.36 ^{+0.17} _{-0.18}	0.01 ^{+0.11} _{-0.10}	0.64 ^{+0.09} _{-0.08}	1.43 ^{+0.01} _{-0.01}	0.83 ^{+0.01} _{-0.01}	2.8 8.5	5011	6117
07276	1.89306e+02	6.21791e+01	2.50 ^{+0.01} _{-0.01}	11.66 ^{+0.12} _{-0.15}	0.14 ^{+0.22} _{-0.23}	0.20 ^{+0.11} _{-0.10}	0.32 ^{+0.08} _{-0.07}	1.50 ^{+0.01} _{-0.01}	0.77 ^{+0.01} _{-0.01}	6.1 14.1	5011	5011
11470	1.89066e+02	6.21987e+01	1.67 ^{+0.01} _{-0.01}	11.08 ^{+0.13} _{-0.14}	0.32 ^{+0.19} _{-0.19}	0.08 ^{+0.10} _{-0.11}	0.13 ^{+0.10} _{-0.10}	1.17 ^{+0.01} _{-0.01}	0.50 ^{+0.01} _{-0.01}	3.0 20.1	10023	8723
17735	1.89061e+02	6.22290e+01	1.84 ^{+0.01} _{-0.01}	11.33 ^{+0.13} _{-0.13}	0.37 ^{+0.19} _{-0.19}	0.13 ^{+0.15} _{-0.14}	0.51 ^{+0.10} _{-0.11}	1.46 ^{+0.01} _{-0.01}	0.83 ^{+0.00} _{-0.00}	3.8 23.5	5011	8123
19341	1.89087e+02	6.22367e+01	1.86 ^{+0.01} _{-0.01}	10.97 ^{+0.15} _{-0.15}	0.03 ^{+0.23} _{-0.23}	0.29 ^{+0.11} _{-0.09}	0.04 ^{+0.04} _{-0.04}	1.19 ^{+0.01} _{-0.01}	0.57 ^{+0.01} _{-0.01}	4.1 31.1	5011	38494
19850	1.89090e+02	6.22392e+01	1.86 ^{+0.01} _{-0.01}	11.05 ^{+0.15} _{-0.15}	0.25 ^{+0.21} _{-0.21}	0.15 ^{+0.13} _{-0.12}	0.53 ^{+0.12} _{-0.14}	1.59 ^{+0.01} _{-0.01}	0.90 ^{+0.01} _{-0.01}	2.1 22.2	5011	38494
22774	1.89128e+02	6.22537e+01	2.01 ^{+0.01} _{-0.01}	11.36 ^{+0.12} _{-0.13}	0.14 ^{+0.17} _{-0.18}	0.15 ^{+0.11} _{-0.09}	0.78 ^{+0.09} _{-0.13}	1.64 ^{+0.01} _{-0.01}	0.97 ^{+0.01} _{-0.01}	2.2 18.4	4811	31476
23006	1.89351e+02	6.22547e+01	2.48 ^{+0.01} _{-0.01}	11.11 ^{+0.13} _{-0.13}	0.13 ^{+0.21} _{-0.22}	0.18 ^{+0.10} _{-0.10}	0.06 ^{+0.07} _{-0.07}	1.27 ^{+0.01} _{-0.01}	0.53 ^{+0.01} _{-0.01}	2.8 8.3	5011	4911
23249	1.89064e+02	6.22560e+01	2.37 ^{+0.01} _{-0.01}	10.89 ^{+0.15} _{-0.15}	0.12 ^{+0.23} _{-0.28}	0.21 ^{+0.18} _{-0.29}	0.33 ^{+0.18} _{-0.21}	1.28 ^{+0.01} _{-0.01}	0.56 ^{+0.02} _{-0.03}	2.9 7.7	5011	15841
24033	1.89115e+02	6.22594e+01	1.67 ^{+0.01} _{-0.01}	11.23 ^{+0.15} _{-0.17}	0.45 ^{+0.21} _{-0.18}	0.18 ^{+0.11} _{-0.10}	0.27 ^{+0.09} _{-0.08}	1.54 ^{+0.01} _{-0.01}	0.87 ^{+0.00} _{-0.00}	3.2 29.2	4811	39494
33780	1.89202e+02	6.23172e+01	1.87 ^{+0.01} _{-0.01}	11.70 ^{+0.20} _{-0.18}	0.48 ^{+0.23} _{-0.23}	0.30 ^{+0.09} _{-0.09}	0.51 ^{+0.11} _{-0.12}	1.92 ^{+0.01} _{-0.01}	1.31 ^{+0.01} _{-0.01}	2.9 14.8	33282	14635
GOODS-South												
09704	5.32857e+01	-2.78641e+01	1.74 ^{+0.01} _{-0.01}	11.71 ^{+0.14} _{-0.14}	0.41 ^{+0.19} _{-0.17}	0.28 ^{+0.12} _{-0.11}	0.69 ^{+0.16} _{-0.19}	1.69 ^{+0.02} _{-0.02}	1.14 ^{+0.00} _{-0.00}	12.5 17.4	98073	4711
23073	5.31231e+01	-2.78034e+01	2.34 ^{+0.01} _{-0.01}	11.32 ^{+0.15} _{-0.17}	0.34 ^{+0.22} _{-0.19}	0.10 ^{+0.10} _{-0.10}	0.16 ^{+0.08} _{-0.09}	1.46 ^{+0.01} _{-0.01}	0.68 ^{+0.01} _{-0.01}	5.4 11.9	0	9423
24569	5.31588e+01	-2.77972e+01	1.90 ^{+0.01} _{-0.01}	11.16 ^{+0.17} _{-0.16}	-0.15 ^{+0.24} _{-0.24}	0.35 ^{+0.10} _{-0.09}	0.20 ^{+0.07} _{-0.08}	1.55 ^{+0.00} _{-0.01}	0.77 ^{+0.01} _{-0.01}	1.0 22.6	103246	23358
31397	5.31410e+01	-2.77667e+01	1.91 ^{+0.01} _{-0.01}	11.51 ^{+0.21} _{-0.21}	0.44 ^{+0.28} _{-0.25}	0.15 ^{+0.08} _{-0.08}	0.38 ^{+0.09} _{-0.09}	1.66 ^{+0.00} _{-0.00}	0.94 ^{+0.00} _{-0.00}	5.9 32.3	0	21552
39364	5.30628e+01	-2.77265e+01	1.61 ^{+0.01} _{-0.01}	11.51 ^{+0.24} _{-0.19}	0.18 ^{+0.24} _{-0.23}	0.44 ^{+0.12} _{-0.17}	0.22 ^{+0.07} _{-0.07}	1.62 ^{+0.01} _{-0.01}	1.09 ^{+0.00} _{-0.00}	8.9 23.6	27270	8923
41021	5.31874e+01	-2.77192e+01	2.32 ^{+0.01} _{-0.01}	11.28 ^{+0.12} _{-0.12}	0.07 ^{+0.18} _{-0.17}	0.15 ^{+0.11} _{-0.11}	0.27 ^{+0.10} _{-0.11}	1.23 ^{+0.01} _{-0.01}	0.54 ^{+0.01} _{-0.01}	4.9 15.7	0	4711
41148	5.31279e+01	-2.77189e+01	1.76 ^{+0.01} _{-0.01}	11.48 ^{+0.20} _{-0.22}	0.34 ^{+0.27} _{-0.26}	0.40 ^{+0.10} _{-0.10}	0.09 ^{+0.07} _{-0.07}	1.87 ^{+0.02} _{-0.02}	1.18 ^{+0.01} _{-0.01}	3.4 10.6	23058	4611
41520	5.31527e+01	-2.77163e+01	1.60 ^{+0.01} _{-0.01}	11.31 ^{+0.25} _{-0.23}	0.19 ^{+0.28} _{-0.27}	0.47 ^{+0.12} _{-0.17}	0.14 ^{+0.07} _{-0.07}	1.81 ^{+0.01} _{-0.01}	1.18 ^{+0.00} _{-0.00}	4.7 10.2	27470	4711
43005	5.31085e+01	-2.77101e+01	1.60 ^{+0.01} _{-0.01}	11.31 ^{+0.22} _{-0.22}	0.40 ^{+0.27} _{-0.28}	0.27 ^{+0.10} _{-0.09}	0.39 ^{+0.07} _{-0.08}	1.82 ^{+0.00} _{-0.01}	1.12 ^{+0.00} _{-0.00}	3.9 13.1	23058	9323
43114	5.30624e+01	-2.77069e+01	1.90 ^{+0.01} _{-0.01}	12.03 ^{+0.20} _{-0.17}	0.09 ^{+0.21} _{-0.20}	0.38 ^{+0.10} _{-0.10}	0.27 ^{+0.07} _{-0.07}	1.45 ^{+0.00} _{-0.00}	0.81 ^{+0.00} _{-0.00}	25.2 49.4	27270	7720

Note. —

^a Average signal-to-noise ratios of grism spectral element measured at blue (3400-3800 Å) and red (4200-5000 Å) wavelength ranges.

^b Total exposure time in G102 and G141 observations.

^c $Z_\odot = 0.0142$ (Asplund et al. 2009).

^d Stellar masses are corrected for magnifications by the foreground cluster.

Table 2
Summary of physical parameters with different SFHs.

Obj ID	gsf ^a			Exponential model					Delayed exponential model				
	χ^2/ν	$\log Z_L^b$ (Z_\odot)	$\log T_L^b$ (Gyr)	χ^2/ν	$\log M_*$ (M_\odot)	$\log Z_L$ (Z_\odot)	$\log T_L$ (Gyr)	A_V (mag)	χ^2/ν	$\log M_*$ (M_\odot)	$\log Z_L$ (Z_\odot)	$\log T_L$ (Gyr)	A_V (mag)
00141	2.41	$0.47^{+0.16}_{-0.17}$	$0.45^{+0.12}_{-0.11}$	2.43	$11.49^{+0.03}_{-0.04}$	$0.54^{+0.04}_{-0.04}$	$-0.61^{+0.04}_{-0.04}$	$1.94^{+0.06}_{-0.07}$	2.47	$11.46^{+0.01}_{-0.02}$	$0.55^{+0.04}_{-0.04}$	$-0.59^{+0.04}_{-0.04}$	$1.95^{+0.03}_{-0.06}$
00227	1.75	$-0.17^{+0.11}_{-0.10}$	$0.68^{+0.26}_{-0.17}$	3.52	$11.02^{+0.09}_{-0.01}$	$-0.30^{+0.14}_{-0.14}$	$-0.41^{+0.05}_{-0.07}$	$0.93^{+0.10}_{-0.01}$	3.95	$10.96^{+0.01}_{-0.03}$	$-0.28^{+0.12}_{-0.15}$	$-0.39^{+0.05}_{-0.04}$	$0.85^{+0.01}_{-0.14}$
06215	1.59	$0.40^{+0.16}_{-0.13}$	$0.79^{+0.21}_{-0.14}$	1.77	$11.48^{+0.01}_{-0.01}$	$0.01^{+0.07}_{-0.07}$	$-0.47^{+0.08}_{-0.06}$	$1.14^{+0.01}_{-0.04}$	1.65	$11.49^{+0.01}_{-0.04}$	$0.05^{+0.15}_{-0.10}$	$-0.40^{+0.04}_{-0.04}$	$1.11^{+0.01}_{-0.04}$
07276	1.54	$0.15^{+0.20}_{-0.21}$	$1.40^{+0.42}_{-0.29}$	2.58	$11.57^{+0.00}_{-0.00}$	$0.00^{+0.07}_{-0.07}$	$0.10^{+0.03}_{-0.03}$	$0.23^{+0.01}_{-0.01}$	2.50	$11.52^{+0.00}_{-0.00}$	$-0.42^{+0.08}_{-0.08}$	$0.21^{+0.04}_{-0.04}$	$0.18^{+0.01}_{-0.01}$
09704	1.74	$0.39^{+0.16}_{-0.15}$	$1.39^{+0.46}_{-0.31}$	3.34	$11.59^{+0.00}_{-0.02}$	$0.54^{+0.04}_{-0.04}$	$-0.29^{+0.06}_{-0.04}$	$1.27^{+0.01}_{-0.08}$	2.72	$11.58^{+0.00}_{-0.00}$	$0.55^{+0.04}_{-0.04}$	$-0.20^{+0.04}_{-0.04}$	$1.18^{+0.01}_{-0.01}$
11470	1.88	$0.32^{+0.15}_{-0.15}$	$0.78^{+0.23}_{-0.17}$	2.65	$11.05^{+0.00}_{-0.00}$	$0.20^{+0.07}_{-0.07}$	$-0.10^{+0.03}_{-0.03}$	$0.27^{+0.00}_{-0.00}$	5.59	$11.03^{+0.03}_{-0.00}$	$0.50^{+0.06}_{-0.14}$	$-0.10^{+0.03}_{-0.03}$	$0.14^{+0.09}_{-0.01}$
17735	1.70	$0.41^{+0.16}_{-0.16}$	$0.92^{+0.35}_{-0.20}$	6.68	$11.28^{+0.01}_{-0.00}$	$0.04^{+0.50}_{-0.10}$	$-0.22^{+0.05}_{-0.07}$	$0.87^{+0.00}_{-0.04}$	2.24	$11.27^{+0.00}_{-0.00}$	$0.40^{+0.07}_{-0.07}$	$-0.20^{+0.04}_{-0.04}$	$0.81^{+0.00}_{-0.00}$
19341	4.37	$0.09^{+0.15}_{-0.16}$	$1.54^{+0.50}_{-0.34}$	20.66	$10.79^{+0.00}_{-0.01}$	$-0.40^{+0.07}_{-0.07}$	$-0.50^{+0.04}_{-0.03}$	$0.73^{+0.01}_{-0.01}$	4.79	$10.79^{+0.00}_{-0.01}$	$-0.41^{+0.07}_{-0.07}$	$-0.49^{+0.04}_{-0.04}$	$0.73^{+0.01}_{-0.01}$
19850	1.87	$0.28^{+0.21}_{-0.22}$	$1.15^{+0.37}_{-0.26}$	4.63	$11.05^{+0.00}_{-0.00}$	$-0.75^{+0.03}_{-0.03}$	$-0.10^{+0.03}_{-0.03}$	$1.03^{+0.01}_{-0.01}$	2.43	$11.03^{+0.03}_{-0.03}$	$0.26^{+0.28}_{-0.17}$	$-0.03^{+0.05}_{-0.08}$	$0.63^{+0.10}_{-0.04}$
22774	1.19	$0.18^{+0.17}_{-0.18}$	$1.20^{+0.34}_{-0.21}$	2.11	$11.36^{+0.00}_{-0.00}$	$-0.75^{+0.03}_{-0.03}$	$-0.10^{+0.03}_{-0.03}$	$1.13^{+0.01}_{-0.01}$	1.59	$11.33^{+0.00}_{-0.00}$	$-0.19^{+0.08}_{-0.08}$	$-0.10^{+0.04}_{-0.04}$	$0.98^{+0.03}_{-0.03}$
23006	1.06	$0.19^{+0.19}_{-0.18}$	$1.18^{+0.31}_{-0.22}$	1.52	$11.03^{+0.05}_{-0.01}$	$-0.64^{+0.09}_{-0.10}$	$-0.00^{+0.04}_{-0.04}$	$0.19^{+0.02}_{-0.05}$	1.34	$11.05^{+0.05}_{-0.02}$	$-0.66^{+0.11}_{-0.10}$	$0.00^{+0.03}_{-0.04}$	$0.23^{+0.06}_{-0.08}$
23073	1.19	$0.36^{+0.21}_{-0.20}$	$1.18^{+0.30}_{-0.24}$	3.62	$11.29^{+0.03}_{-0.00}$	$0.25^{+0.16}_{-0.10}$	$-0.02^{+0.05}_{-0.08}$	$0.21^{+0.10}_{-0.01}$	2.66	$11.30^{+0.00}_{-0.00}$	$0.41^{+0.08}_{-0.08}$	$-0.01^{+0.04}_{-0.04}$	$0.22^{+0.01}_{-0.01}$
23249	1.48	$0.21^{+0.20}_{-0.23}$	$1.20^{+0.78}_{-0.57}$	1.52	$10.81^{+0.02}_{-0.01}$	$0.41^{+0.12}_{-0.12}$	$-0.53^{+0.06}_{-0.08}$	$0.77^{+0.06}_{-0.02}$	1.45	$10.80^{+0.05}_{-0.08}$	$0.47^{+0.10}_{-0.14}$	$-0.50^{+0.12}_{-0.11}$	$0.77^{+0.06}_{-0.13}$
24033	2.18	$0.44^{+0.18}_{-0.18}$	$1.27^{+0.29}_{-0.24}$	20.81	$11.15^{+0.00}_{-0.00}$	$0.21^{+0.08}_{-0.08}$	$-0.01^{+0.04}_{-0.04}$	$0.48^{+0.01}_{-0.01}$	5.73	$11.16^{+0.00}_{-0.00}$	$0.40^{+0.07}_{-0.07}$	$0.00^{+0.03}_{-0.03}$	$0.48^{+0.00}_{-0.00}$
24569	2.66	$-0.08^{+0.23}_{-0.22}$	$2.09^{+0.55}_{-0.42}$	6.03	$10.91^{+0.01}_{-0.00}$	$-0.20^{+0.07}_{-0.07}$	$0.10^{+0.03}_{-0.03}$	$0.03^{+0.03}_{-0.01}$	5.16	$10.91^{+0.01}_{-0.01}$	$-0.20^{+0.07}_{-0.07}$	$0.10^{+0.03}_{-0.03}$	$0.05^{+0.03}_{-0.02}$
31397	2.81	$0.44^{+0.24}_{-0.23}$	$1.28^{+0.29}_{-0.22}$	8.22	$11.48^{+0.00}_{-0.04}$	$0.36^{+0.09}_{-0.14}$	$0.02^{+0.08}_{-0.05}$	$0.52^{+0.01}_{-0.16}$	4.89	$11.48^{+0.00}_{-0.00}$	$0.41^{+0.07}_{-0.08}$	$0.10^{+0.04}_{-0.04}$	$0.41^{+0.01}_{-0.01}$
33780	1.72	$0.47^{+0.22}_{-0.22}$	$1.84^{+0.38}_{-0.36}$	2.95	$11.55^{+0.00}_{-0.00}$	$-0.75^{+0.03}_{-0.03}$	$0.00^{+0.03}_{-0.03}$	$1.35^{+0.01}_{-0.01}$	1.81	$11.66^{+0.03}_{-0.03}$	$-0.27^{+0.12}_{-0.16}$	$0.35^{+0.07}_{-0.07}$	$0.67^{+0.13}_{-0.10}$
39364	3.98	$0.17^{+0.20}_{-0.19}$	$2.24^{+0.82}_{-0.66}$	6.42	$11.44^{+0.00}_{-0.00}$	$-0.61^{+0.09}_{-0.09}$	$0.00^{+0.03}_{-0.03}$	$1.19^{+0.00}_{-0.05}$	7.11	$11.45^{+0.00}_{-0.04}$	$-0.56^{+0.13}_{-0.09}$	$0.00^{+0.04}_{-0.04}$	$1.24^{+0.00}_{-0.06}$
41021	2.86	$0.19^{+0.15}_{-0.15}$	$1.04^{+0.32}_{-0.23}$	3.22	$11.19^{+0.01}_{-0.12}$	$0.13^{+0.15}_{-0.86}$	$-0.47^{+0.38}_{-0.10}$	$0.71^{+0.05}_{-0.31}$	3.00	$11.29^{+0.03}_{-0.00}$	$-0.72^{+0.95}_{-0.06}$	$-0.13^{+0.06}_{-0.38}$	$0.41^{+0.32}_{-0.01}$
41148	2.36	$0.35^{+0.27}_{-0.26}$	$2.46^{+0.68}_{-0.50}$	3.65	$11.56^{+0.00}_{-0.00}$	$0.20^{+0.07}_{-0.07}$	$0.48^{+0.02}_{-0.02}$	$0.00^{+0.00}_{-0.00}$	3.77	$11.55^{+0.00}_{-0.00}$	$0.20^{+0.07}_{-0.07}$	$0.47^{+0.02}_{-0.02}$	$0.00^{+0.00}_{-0.00}$
41520	1.94	$0.18^{+0.27}_{-0.26}$	$2.86^{+0.95}_{-0.92}$	2.88	$11.36^{+0.00}_{-0.00}$	$0.20^{+0.07}_{-0.07}$	$0.48^{+0.02}_{-0.02}$	$0.06^{+0.01}_{-0.01}$	2.71	$11.35^{+0.01}_{-0.00}$	$0.20^{+0.07}_{-0.07}$	$0.47^{+0.02}_{-0.02}$	$0.06^{+0.01}_{-0.01}$
43005	2.73	$0.40^{+0.26}_{-0.28}$	$1.85^{+0.46}_{-0.33}$	3.27	$11.20^{+0.00}_{-0.00}$	$0.55^{+0.03}_{-0.03}$	$0.20^{+0.03}_{-0.03}$	$0.05^{+0.01}_{-0.01}$	4.81	$11.21^{+0.00}_{-0.00}$	$0.55^{+0.03}_{-0.03}$	$0.20^{+0.03}_{-0.03}$	$0.05^{+0.01}_{-0.01}$
43114	8.08	$0.24^{+0.17}_{-0.15}$	$1.76^{+0.35}_{-0.40}$	12.98	$11.99^{+0.02}_{-0.00}$	$-0.42^{+0.08}_{-0.13}$	$-0.10^{+0.03}_{-0.04}$	$0.81^{+0.06}_{-0.00}$	17.93	$11.95^{+0.03}_{-0.01}$	$-0.55^{+0.16}_{-0.10}$	$-0.17^{+0.08}_{-0.05}$	$0.92^{+0.04}_{-0.01}$

Note. —

^aStellar mass and dust attenuation for gsf are listed in Table 1.

^bLight-weighted metallicity and age, to match those derived with functional SFHs.

REFERENCES

- Abramson, L. E., & Morishita, T. 2018, *ApJ*, 858, 40
- Abramson, L. E., Newman, A. B., Treu, T., et al. 2018, *AJ*, 156, 29
- Andrews, B. H., & Martini, P. 2013, *ApJ*, 765, 140
- Asplund, M., Grevesse, N., Sauval, A. J., & Scott, P. 2009, *ARA&A*, 47, 481
- Balogh, M. L., Morris, S. L., Yee, H. K. C., Carlberg, R. G., & Ellingson, E. 1999, *ApJ*, 527, 54
- Barro, G., Faber, S. M., Pérez-González, P. G., et al. 2013, *ApJ*, 765, 104
- , 2014, *ApJ*, 791, 52
- Bell, E. F., McIntosh, D. H., Katz, N., & Weinberg, M. D. 2003, *ApJS*, 149, 289
- Belli, S., Newman, A. B., & Ellis, R. S. 2014, *ApJ*, 783, 117
- , 2017, *ApJ*, 834, 18
- , 2018, *ArXiv e-prints*, arXiv:1810.00008
- Bertin, E., & Arnouts, S. 1996, *A&AS*, 117, 393
- Boquien, M., Buat, V., & Perret, V. 2014, *A&A*, 571, A72
- Brammer, G. 2018, *gbrammer/grizli*: Preliminary release, doi:10.5281/zenodo.1146905
- Brammer, G. B., Marchesini, D., Labbé, I., et al. 2016, *ApJS*, 226, 6
- Calzetti, D., Armus, L., Bohlin, R. C., et al. 2000, *ApJ*, 533, 682
- Carnall, A. C., Leja, J., Johnson, B. D., et al. 2018, *ArXiv e-prints*, arXiv:1811.03635
- Chauke, P., van der Wel, A., Pacifici, C., et al. 2018, *ApJ*, 861, 13
- Choi, J., Conroy, C., Moustakas, J., et al. 2014, *ApJ*, 792, 95
- Choi, J., Dotter, A., Conroy, C., et al. 2016, *ApJ*, 823, 102
- Cid Fernandes, R. 2018, *ArXiv e-prints*, arXiv:1807.10423
- Cid Fernandes, R., Mateus, A., Sodré, L., Stasińska, G., & Gomes, J. M. 2005, *MNRAS*, 358, 363
- Cole, S., Norberg, P., Baugh, C. M., et al. 2001, *MNRAS*, 326, 255
- Conroy, C. 2013, *ARA&A*, 51, 393
- Conroy, C., & Gunn, J. E. 2010, *ApJ*, 712, 833
- Conroy, C., Gunn, J. E., & White, M. 2009, *ApJ*, 699, 486
- Cowie, L. L., Songaila, A., Hu, E. M., & Cohen, J. G. 1996, *AJ*, 112, 839
- Daddi, E., Renzini, A., Pirzkal, N., et al. 2005, *ApJ*, 626, 680
- de Jong, R. S. 1996, *A&A*, 313, 377
- Dekel, A., & Birnboim, Y. 2006, *MNRAS*, 368, 2
- Diemer, B., Sparre, M., Abramson, L. E., & Torrey, P. 2017, *ApJ*, 839, 26
- Dressler, A., & Gunn, J. E. 1983, *ApJ*, 270, 7
- Dressler, A., Kelson, D. D., & Abramson, L. E. 2018, *ArXiv e-prints*, arXiv:1805.04110
- Dressler, A., Kelson, D. D., Abramson, L. E., et al. 2016, *ApJ*, 833, 251
- Erb, D. K., Shapley, A. E., Pettini, M., et al. 2006, *ApJ*, 644, 813
- Estrada-Carpenter, V., Papovich, C., Momcheva, I., et al. 2018, *ArXiv e-prints*, arXiv:1810.02824
- Feldmann, R., & Mayer, L. 2015, *MNRAS*, 446, 1939
- Foreman-Mackey, D., Hogg, D. W., Lang, D., & Goodman, J. 2013, *PASP*, 125, 306
- Foreman-Mackey, D., Sick, J., & Johnson, B. 2014, doi:10.5281/zenodo.12157
- Franco, M., Elbaz, D., Béthermin, M., et al. 2018, *ArXiv e-prints*, arXiv:1803.00157
- Fukugita, M., Ichikawa, T., Gunn, J. E., et al. 1996, *AJ*, 111, 1748
- Gallazzi, A., Bell, E. F., Zibetti, S., Brinchmann, J., & Kelson, D. D. 2014, *ApJ*, 788, 72
- Gallazzi, A., Charlot, S., Brinchmann, J., White, S. D. M., & Tremonti, C. A. 2005, *MNRAS*, 362, 41
- Glazebrook, K., Schreiber, C., Labbé, I., et al. 2017, *Nature*, 544, 71
- Gobat, R., Daddi, E., Strazzullo, V., et al. 2017, *A&A*, 599, A95
- Gobat, R., Daddi, E., Magdis, G., et al. 2018, *Nature Astronomy*, 2, 239
- González Delgado, R. M., Cid Fernandes, R., García-Benito, R., et al. 2014, *ApJ*, 791, L16
- Grogin, N. A., Kocevski, D. D., Faber, S. M., et al. 2011, *ApJS*, 197, 35
- Hamann, F., & Ferland, G. 1999, *ARA&A*, 37, 487
- Heavens, A., Panter, B., Jimenez, R., & Dunlop, J. 2004, *Nature*, 428, 625
- Hopkins, P. F., Hernquist, L., Cox, T. J., Keres, D., & Wuyts, S. 2009, *ApJ*, 691, 1424
- Iyer, K., & Gawiser, E. 2017, *ApJ*, 838, 127
- Jimenez, R., Bernardi, M., Haiman, Z., Panter, B., & Heavens, A. F. 2007, *ApJ*, 669, 947
- Juneau, S., Bournaud, F., Charlot, S., et al. 2014, *ApJ*, 788, 88
- Kauffmann, G., Heckman, T. M., White, S. D. M., et al. 2003, *MNRAS*, 341, 33
- Kaviraj, S., Tan, K.-M., Ellis, R. S., & Silk, J. 2011, *MNRAS*, 411, 2148
- Kelly, P. L., Rodney, S. A., Treu, T., et al. 2015, *Science*, 347, 1123
- Kelly, P. L., Brammer, G., Selsing, J., et al. 2016, *ApJ*, 831, 205
- Kelson, D. D., Williams, R. J., Dressler, A., et al. 2014, *ApJ*, 783, 110
- Kennicutt, Jr., R. C. 1998, *ARA&A*, 36, 189
- Kewley, L. J., & Ellison, S. L. 2008, *ApJ*, 681, 1183
- Kirby, E. N., Cohen, J. G., Guhathakurta, P., et al. 2013, *ApJ*, 779, 102
- Koekemoer, A. M., Faber, S. M., Ferguson, H. C., et al. 2011, *ApJS*, 197, 36
- Kriek, M., van Dokkum, P. G., Labbé, I., et al. 2009, *ApJ*, 700, 221
- Kriek, M., Conroy, C., van Dokkum, P. G., et al. 2016, *Nature*, 540, 248
- Larson, R. B., Tinsley, B. M., & Caldwell, C. N. 1980, *ApJ*, 237, 692
- Leethochawalit, N., Kirby, E. N., Moran, S. M., Ellis, R. S., & Treu, T. 2018, *ApJ*, 856, 15
- Lehner, N., O'Meara, J. M., Howk, J. C., Prochaska, J. X., & Fumagalli, M. 2016, *ApJ*, 833, 283
- Leja, J., Carnall, A. C., Johnson, B. D., Conroy, C., & Speagle, J. S. 2018, *ArXiv e-prints*, arXiv:1811.03637
- Lilly, S. J., & Carollo, C. M. 2016, *ApJ*, 833, 1
- Lonoce, I., Longhetti, M., Maraston, C., et al. 2015, *MNRAS*, 454, 3912
- Lotz, J. M., Jonsson, P., Cox, T. J., et al. 2011, *ApJ*, 742, 103
- Lotz, J. M., Koekemoer, A., Coe, D., et al. 2017, *ApJ*, 837, 97
- Maiolino, R., Nagao, T., Grazian, A., et al. 2008, *A&A*, 488, 463
- Man, A., & Belli, S. 2018, *Nature Astronomy*, 2, 695
- Mannucci, F., Cresci, G., Maiolino, R., Marconi, A., & Gnerucci, A. 2010, *MNRAS*, 408, 2115
- Marsan, Z. C., Marchesini, D., Brammer, G. B., et al. 2015, *ApJ*, 801, 133
- Martin-Navarro, I., Vazdekis, A., Falcón-Barroso, J., et al. 2018, *MNRAS*, 475, 3700
- McDermid, R. M., Alatalo, K., Blitz, L., et al. 2015, *MNRAS*, 448, 3484
- Momcheva, I. G., Brammer, G. B., van Dokkum, P. G., et al. 2016, *ApJS*, 225, 27
- Morishita, T., & Ichikawa, T. 2016, *ApJ*, 816, 87
- Morishita, T., Ichikawa, T., & Kajisawa, M. 2014, *ApJ*, 785, 18
- Morishita, T., Ichikawa, T., Noguchi, M., et al. 2015, *ApJ*, 805, 34
- Morishita, T., Abramson, L. E., Treu, T., et al. 2017, *ApJ*, 835, 254
- , 2018, *ApJ*, 856, L4
- Muna, D., Alexander, M., Allen, A., et al. 2016, *ArXiv e-prints*, arXiv:1610.03159
- Muzzin, A., Marchesini, D., Stefanon, M., et al. 2013, *ApJ*, 777, 18
- Naab, T., Johansson, P. H., & Ostriker, J. P. 2009, *ApJ*, 699, L178
- Newman, A. B., Ellis, R. S., Bundy, K., & Treu, T. 2012, *ApJ*, 746, 162
- Newville, M., Nelson, A., Ingargiola, A., et al. 2017, doi:10.5281/zenodo.802298
- Nipoti, C., Treu, T., Leauthaud, A., et al. 2012, *MNRAS*, 422, 1714
- Oesch, P. A., Montes, M., Reddy, N., et al. 2018, *ArXiv e-prints*, arXiv:1806.01853
- Oke, J. B., & Gunn, J. E. 1983, *ApJ*, 266, 713
- Onodera, M., Renzini, A., Carollo, M., et al. 2012, *ApJ*, 755, 26
- Onodera, M., Carollo, C. M., Renzini, A., et al. 2015, *The Astrophysical Journal*, 808, 161
- Onodera, M., Carollo, C. M., Lilly, S., et al. 2016, *ApJ*, 822, 42
- Oser, L., Ostriker, J. P., Naab, T., Johansson, P. H., & Burkert, A. 2010, *ApJ*, 725, 2312
- Osterbrock, D. E. 1989, *Astrophysics of gaseous nebulae and active galactic nuclei*
- Pacifici, C., Kassin, S. A., Weiner, B. J., et al. 2016, *ApJ*, 832, 79
- Panther, B., Jimenez, R., Heavens, A. F., & Charlot, S. 2007, *MNRAS*, 378, 1550
- , 2008, *MNRAS*, 391, 1117
- Peng, Y., Maiolino, R., & Cochrane, R. 2015, *Nature*, 521, 192
- Pirzkal, N., Malhotra, S., Ryan, R. E., et al. 2017, *ApJ*, 846, 84
- Poggianti, B. M., Calvi, R., Bindoni, D., et al. 2013, *ApJ*, 762, 77
- Postman, M., Coe, D., Benítez, N., et al. 2012, *ApJS*, 199, 25
- Riechers, D. A., Bradford, C. M., Clements, D. L., et al. 2013, *Nature*, 496, 329
- Salpeter, E. E. 1955, *ApJ*, 121, 161
- Schawinski, K., Urry, C. M., Simmons, B. D., et al. 2014, *MNRAS*, 440, 889
- Schmidt, K. B., Treu, T., Brammer, G. B., et al. 2014, *ApJ*, 782, L36
- Schreiber, C., Glazebrook, K., Nanayakkara, T., et al. 2018, *ArXiv e-prints*, arXiv:1807.02523
- Skelton, R. E., Whitaker, K. E., Momcheva, I. G., et al. 2014, *ApJS*, 214, 24
- Smail, I., Kuntschner, H., Kodama, T., et al. 2001, *MNRAS*, 323, 839
- Snyder, G. F., Lotz, J. M., Rodriguez-Gomez, V., et al. 2017, *MNRAS*, 468, 207
- Straatman, C. M. S., Labbé, I., Spitler, L. R., et al. 2014, *ApJ*, 783, L14
- Tacconi, L. J., Genzel, R., Smail, I., et al. 2008, *ApJ*, 680, 246
- Taylor, E. N., Franx, M., Glazebrook, K., et al. 2010, *ApJ*, 720, 723
- Teplitz, H. I., Rafelski, M., Kurczynski, P., et al. 2013, *AJ*, 146, 159
- Thomas, D., Maraston, C., & Bender, R. 2003, *MNRAS*, 339, 897
- Thomas, D., Maraston, C., Bender, R., & Mendes de Oliveira, C. 2005, *ApJ*, 621, 673
- Thomas, D., Maraston, C., Schawinski, K., Sarzi, M., & Silk, J. 2010, *MNRAS*, 404, 1775
- Toft, S., Smolčić, V., Magnelli, B., et al. 2014, *ApJ*, 782, 68
- Tojeiro, R., Heavens, A. F., Jimenez, R., & Panter, B. 2007, *MNRAS*, 381, 1252
- Tomczak, A. R., Quadri, R. F., Tran, K.-V. H., et al. 2014, *ApJ*, 783, 85
- Torrey, P., Cox, T. J., Kewley, L., & Hernquist, L. 2012, *ApJ*, 746, 108
- Torrey, P., Wellons, S., Ma, C.-P., Hopkins, P. F., & Vogelsberger, M. 2017, *MNRAS*, 467, 4872
- Trager, S. C., Faber, S. M., Worthey, G., & González, J. J. 2000, *AJ*, 119, 1645
- Tremonti, C. A., Heckman, T. M., Kauffmann, G., et al. 2004, *ApJ*, 613, 898
- Treu, T., Ellis, R. S., Liao, T. X., & van Dokkum, P. G. 2005a, *ApJ*, 622, L5
- Treu, T., Ellis, R. S., Liao, T. X., et al. 2005b, *ApJ*, 633, 174
- Treu, T., Schmidt, K. B., Brammer, G. B., et al. 2015, *ApJ*, 812, 114
- Truncoso, P., Maiolino, R., Sommariva, V., et al. 2014, *A&A*, 563, A58
- Trujillo, I., Conselice, C. J., Bundy, K., et al. 2007, *MNRAS*, 382, 109
- van der Wel, A., Franx, M., van Dokkum, P. G., et al. 2014, *ApJ*, 788, 28

- van Dokkum, P., Brammer, G., Momcheva, I., et al. 2013a, ArXiv e-prints, arXiv:1305.2140
- van Dokkum, P. G., Franx, M., Kriek, M., et al. 2008, ApJ, 677, L5
- van Dokkum, P. G., Leja, J., Nelson, E. J., et al. 2013b, ApJ, 771, L35
- van Dokkum, P. G., Nelson, E. J., Franx, M., et al. 2015, ApJ, 813, 23
- Vazdekis, A., Coelho, P., Cassisi, S., et al. 2015, MNRAS, 449, 1177
- Verma, A., Lehnert, M. D., Förster Schreiber, N. M., Bremer, M. N., & Douglas, L. 2007, MNRAS, 377, 1024
- Walcher, C. J., Coelho, P., Gallazzi, A., & Charlot, S. 2009, MNRAS, 398, L44
- Walcher, C. J., Coelho, P. R. T., Gallazzi, A., et al. 2015, A&A, 582, A46
- Wang, X., Jones, T. A., Treu, T., et al. 2017, ApJ, 837, 89
- . 2018, ArXiv e-prints, arXiv:1808.08800
- Wellons, S., Torrey, P., Ma, C.-P., et al. 2015, MNRAS, 449, 361
- Whitaker, K. E., van Dokkum, P. G., Brammer, G., et al. 2013, ApJ, 770, L39
- Whitaker, K. E., Bezanson, R., van Dokkum, P. G., et al. 2017, ApJ, 838, 19
- Williams, R. J., Quadri, R. F., Franx, M., van Dokkum, P., & Labbé, I. 2009, ApJ, 691, 1879
- Worthey, G. 1994, ApJS, 95, 107
- Wuyts, S., Förster Schreiber, N. M., Genzel, R., et al. 2012, ApJ, 753, 114
- Yabe, K., Ohta, K., Iwamuro, F., et al. 2014, MNRAS, 437, 3647
- Yi, S., Demarque, P., & Oemler, Jr., A. 1997, ApJ, 486, 201
- Younger, J. D., Fazio, G. G., Huang, J.-S., et al. 2007, ApJ, 671, 1531
- Zahid, H. J., Kashino, D., Silverman, J. D., et al. 2014, ApJ, 792, 75